Alma Mater Studiorum
Università di Bologna

Dottorato di Ricerca in Fisica
XXIV Ciclo

Electron identification and reconstruction with the OPERA ECC bricks and search for $\nu_\mu \rightarrow \nu_e$ oscillations

settore concorsuale di afferenza: 02/A1
settore scientifico disciplinare: FIS/04

Author:
Matteo Tenti

Advisor:
Prof. Maximiliano Sioli

PhD Coordinator:
Prof. Fabio Ortolani

Esame finale anno 2012

Contents

Introduction

During the last decades neutrino physics has done impressive improvements, which led to the classification of neutrino as a fundamental particle in the Standard Model. In this model, it is regarded as a massless particle. Nevertheless, first the problem of solar neutrino deficit, and then the atmospheric neutrino anomaly, observed and confirmed by several experiments using different neutrino sources, seem by now to have a natural explanation in the neutrino oscillation theory: this hypotesis is effective only if neutrinos have a not null mass and if mass and flavor eigenstates do not coincide and, therefore, requires an extension of the Standard Model. Despite the fact that there are compelling experimental evidences supporting the oscillation $\nu_\mu \rightarrow \nu_\tau$ in the atmospheric sector, a direct evidence of the ν_τ appearance is still missing. It requires a detector capable of identifying the shortlived τ lepton produced in ν_τ Charged Current interactions. The OPERA detector in Gran Sasso National Laboratory (LNGS) is designed to accomplish this task, aiming at the detection of ν_τ in an almost pure ν_μ beam (CNGS) produced at CERN SPS, 730 km far from the detector. A micrometric detection resolution is needed to identify the short-lived τ lepton; on the other side a large target mass is needed to collect enough statistics. For these reasons, the basic unit of the OPERA detector, the "brick", is based on the concept of ECC (Emulsion Cloud Chamber), a modular structure composed by high-density passive material (lead) and nuclear emulsion sheets, as high-accuracy tracking devices. Each brick is composed of 56, 1 mm thick, lead plates interleaved with nuclear emulsion films for a total weight of 8.3 kg; $\sim$ 150000

of such target units have been produced for a total mass of 1.25 kton; they have been arranged in vertical "walls", transverse to the beam direction, interleaved with plastic scintillator strips, which have the task to identify the brick where the neutrino interaction occurred. Magnetic spectrometers are used to eventually identify muons and measure their charge and momentum. Two interface emulsion films, called "Changeable Sheets (CS)", are attached to the downstream side of each brick and can be removed without opening the brick: they act as an off-line trigger, to confirm that the brick selected by the electronic detectors is the neutrino interaction one. If tracks related to the neutrino interaction are observed in these CS, the corresponding brick is dismantled and the emulsion sheets developed and sent to the scanning laboratories to be analized. In the laboratories the tracks observed in the CS are followed in the emulsions of the brick, by the "Scanback procedure" until they are no more found. A volume of $1 \times 1\ cm^2$ for 15 films is scanned around the last position of the track in order to reconstruct the interaction vertex. This procedure (standard) is optimazed for high penetrating tracks and is less efficient for showering particles like electron. For this reason new procedure has been defined in order to recover event with an electromagnetic shower in its final state not located with the standard one. The new procedure include the standard procedure during which several electromagnetic shower hint has been defined by means of the available data. In case the event is not located, the presence of an electromagnetic shower hint trigger a dedicated procedure. The old and new location procedure has been then simulated in order to obtain the standard location efficiency and the possible gain due to the new one for the events with electromagnetic shower. Finally a Data-MC comparison has been performed for the 2008 and 2009 runs for what concern the NC in order to validate the Monte Carlo. Then the expected ν_e interactions for the 2008 and 2009 runs has been evaluated and compared with the available data.

Chapter 1

Neutrino Oscillations

1.1 Neutrino History

In 1914 J. Chadwick measured the spectrum of the electrons emitted by β decay of Radium B and C[1] and instead to be discrete as for α and γ two-body decay, unexpectedly it was found to be continuos, so the question of its interpretation was raised.

A crucial experiment was performed by C. D. Ellis and W. A. Wooster in 1927, in which they measured the total energy released in the β decay of Radium E (i.e. ^{210}Bi) source inside a calorimeter thick enough to stop all emitted electrons [2]. The result was in agreement with a continuos electron energy spectrum and excluded the possibility that photon was emitted with the electron. In 1930 L. Maitner and W. Orthman repeated the experiment confirming the previuos result [3]. Following these experimental results, there remained only two theoretical possibilities for the interpretation of the continuos β spectrum:

- The conservation of energy holds only statistically in this particular interaction, which gives rise to β radioactivity.

[1] Historically, the radioactive decay product of radium were labeled Radium A, B, C and so forth [1]. Therefore Radium B and C correspond respectively to ^{214}Pb and ^{214}Bi

- The conservation of energy holds strictly in each primarly process; however, an additional, very penetrating radiation is emitted together with the electrons.

W. Pauli followed the second possibility and in 1930 proposed that this additional radiation was a new particle, called *neutron* by him, with spin 1/2 and a mass not larger than 1% of the proton mass, obeying the exclusion principle [4].

When Chandwick in 1932 discovered the neutron [5] as a neutral component of the nucleus with a mass of the order of that of proton (indeed too large for the Pauli's neutron), Fermi proposed then to call the missing particle of the β decay *neutrino* and in 1934 propesed a theory of the β decay [6] described as a three-body decay, in which neutrino and electron were simultaneously emitted from the nucleus sharing momentum and energy in the process:

$$n \rightarrow p + e^- + \overline{\nu} \tag{1.1}$$

It was the first formulation of a theory explaining a new kind of interaction: the *weak* interaction.

Neutrino was finally detected in 1956 by Cowan and Reines in a nuclear reactor experiment [7]. They observed electron antineutrinos coming from the nuclear reactor interacting with 400 liters of water and cadmium chloride through the process:

$$\overline{\nu} + p \rightarrow n + e^+ \tag{1.2}$$

The $\overline{\nu}$ from the reactor interacted with the protons of the target yelding a neutron and a positron. The target was surrounded by scintillators that detected the light from the positron annihilation and the neutron capture (the same basic method is used today to observe $\overline{\nu}_e$ in nuclear reactors experiments).

In 1958 M. Goldhaber, L. Grodzins and A. W. Sunyar [8] measured the elicity of γ produced in the reaction chain:

$$^{152}Eu + e^- \rightarrow \nu + ^{152}Sm^* \rightarrow ^{152}Sm + \gamma \tag{1.3}$$

It is possible to show that the γ emitted in the opposite direction of neutrino has always its same helicity. Performing the experiment, they found a result compatible with 100% negative helicity for γ and therefore for neutrino.

L. M. Lederman, N. Mistry and J. Steinberger in 1962 [9], observed the topologies of the interactions of the neutrinos produced by the decay on flight of pions according to the reaction:

$$\pi \rightarrow \mu + \nu \tag{1.4}$$

using 10-ton aluminum spark chamber. They demonstrated that ν from π produces μ but do not produces electron and hence are different from neutrino involved in β decay.

In 1975 M. Perl discovered for the first time the creation of $\tau^+\tau^-$ pairs in e^+e^- collisions at SLAC, adding a third leptonic family to the other two [10].

Meanwhile, supposing the universality if the weak interaction, the quark mixing, descrived by CKM (Cabibbo-Kobayashi-Maskawa) matrix, was proposed[11, 12]. Maki, Nakagawa and Sakata, [14] generalizing an idea of Pontecorvo [13], suggested a mixing matrix also for leptons. Only the third lepton family was not yet completed.

In 1973 neutral currents were discovered at CERN and confirmed at Fermilab. A complete knowledge of weak interactions came after the discoveries of the $W^{\pm}$ and the Z^0 bosons in 1983 at the CERN SPS $\overline{p}p$ collider; in 1989 the study of the Z^0 boson width at LEP allowed to show that only three lepton families (and then three types of "light" neutrinos with mass less than half the Z^0 mass) exist [15].

The experimental evidences of ν_τ came in 2001 at Fermilab [16] by the $E872$ experiment, also known as DONUT (Direct Observation of the Nu Tau), through the selection of the events with the characteristic τ decay tracks produced by charged current ν_τ interactions with an iron instrumented target. The third lepton family was then completed.

1.2 Neutrino in the Standard Model

The Standard Model (SM) is a mathematical theory developed throughout the mid to late 20th, concerning the electromagnetic, weak and strong interaction, which mediate the dynamics of the known subatomic particles. The first step was Sheldon Glashow's discovery of a way to combine electromagnetic and weak interactions. In 1967 Steven Weinberg and Abdus Salam incorporated in the SM the Higgs mechanism, belived to give rise to the masses of all the elementary particles. The theory of strong interactions, to which many contributed, acquired its modern form around 1973-74, when experiments confirmed that hadrons were composed of fractionally charged quarks.

Quantum electroweak and quantum chromodynamics are grouped into an internally consistent theory that describes the interactions between particles in terms of quantum field theory. In the formalism of the field theory a particle is represented by a function ψ called field and each fundamental interactions is descibed by a Lagrangian invariant under symmetry group. The $SU(2)_L \otimes U(1)_Y$ concerns the electroweak sector, L index represents the left chirality of the particles and Y index represents the weak hypercharge ($Y = \frac{1}{2}(q - I_3)$, where q is the electric charge and I_3 the third component of the weak isospin). The $SU(3)_C$ group describes the strong interaction in the quark sector and C is the index used to denote the "color" of the particles. So the SM could essentially be defined as $SU(3)_C \otimes SU(2)_L \otimes U(1)_Y$ gauge symmetry.

Fundamental particles in SM are classified into two categories: particles with spin $\frac{1}{2}$ following Fermi-Dirac statistics, called fermions and particles with spin 1 described by Einstein-Bose statistics, known as bosons.

Fermions are classified according to how they interact. There are six quarks (up, down , charm, strange, top, bottom), and six leptons (electron, muon, tau and their relative neutrinos). Pairs from each classification are grouped together to from a generation, with corresponding particles exhibiting similar physical behavior.

The defining property of the quarks is that they carry "color" charge, and hence, interact via the strong interaction. On the other hand the leptons do not have "color" charge; the three neutrinos do not carry electric charge either, so their motion is directly influenced only by the weak force, while electron, muon and tau, by virtue of carrying an electric charge, all interact electromagnetically. As concerns electroweak interaction, fermions are organized in $SU(2)_L$ doublets of left chirality and $U(1)_Y$ singlets of right chirality:

$$\begin{aligned}
1^{st}\ \ generation: &\ \begin{pmatrix} \nu_e \\ e^- \end{pmatrix}_L,\ e_R^-,\ \begin{pmatrix} u \\ d \end{pmatrix}_L,\ u_R,\ d_R \\
2^{nd}\ \ generation: &\ \begin{pmatrix} \nu_\mu \\ \mu^- \end{pmatrix}_L,\ \mu_R^-,\ \begin{pmatrix} c \\ s \end{pmatrix}_L,\ c_R,\ s_R \\
3^{rd}\ \ generation: &\ \begin{pmatrix} \nu_\tau \\ \tau^- \end{pmatrix}_L,\ \tau_R^-,\ \begin{pmatrix} t \\ b \end{pmatrix}_L,\ t_R,\ b_R
\end{aligned} \tag{1.5}$$

It has to be noticed that, due to the fact that neutrino has always been found to be left-handed (and antineutrino right-handed), the right-handed component of neutrino field has not been introduced in SM.

In SM bosons are defined as force carriers that mediate strong, weak and elctromagnetic interactions and are in total 12: the photon for the electromagnetic interaction, $W^\pm$ and Z^0 for the weak interaction and 8 glouns for the strong interactions. The thirteenth boson is the Higgs boson, that has spin 0 and, if exists, would explain why the other elementary particles, the photon and gluon excepted, are massive.

1.3 Neutrino masses

The SM has been precisely confirmed by acceleretor experiment, nevertheless it cannot be considered a complete theory of foundamental interactions. It does not includes gravity, assumes massless neutrino and has some

other problems (such as hierarchy problem, i.e. the not understood large difference between the expected Higgs boson mass and the grand unification scale). Beyond the SM, there are different ways to make neutrino massive:

- By adding a neutrino of right chirality ν_R not included in the SM, the Yukawa coupling with the Higgs boson gives rise to a neutrino mass m_D, called Dirac mass. The corresponding Lagrangian of the Dirac mass is:

$$\mathcal{L}_{m_D} = -m_D \overline{\nu_R} \nu_L + h.c. \tag{1.6}$$

  The leptonic quantum number L is conserved (as well as the leptonic quantum numbers of the families L_e, L_μ and L_τ) and the neutrinos differ from the antineutrinos (they are then called Dirac particles).

- By including a Majorana mass term m_L by coupling a neutrino of left chirality with the Higgs boson. The Lagrangian of Majorana Mass is:

$$\mathcal{L}_{m_L} = -\frac{m_L}{2} \overline{\nu_L^C} \nu_L + h.c., \tag{1.7}$$

  where ν^C is the charge conjugate of ν and fulfills the condition $\nu^C = \nu$. This term brakes the symmetry $U(1)_Y$ and the leptonic number is not conserved. In this case neutrinos are equivalent to antineutrinos (they are then called Majorana particles). If only the ν_L exist, then neutrinos only can have a Majorana mass.

- By adding a Dirac-Majorana term and assuming the considerations of the two first cases, a new Majorana mass term of right chirality m_R is associated to the Lagrangian:

$$\mathcal{L}_{m_R} = -\frac{m_R}{2} \overline{\nu_R^C} \nu_R + h.c. \tag{1.8}$$

  If both ν_L and ν_R exist then neutrinos can have both Majorana and Dirac mass components.

The general Lagrangian can be written as:

$$\begin{aligned}\mathcal{L} &= \mathcal{L}_{m_D} + \mathcal{L}_{m_L} + \mathcal{L}_{m_R} \\ &= -\frac{1}{2}\begin{pmatrix} \overline{\nu_L^C} & \overline{\nu_R} \end{pmatrix}\begin{pmatrix} m_L & m_D \\ m_D & m_R \end{pmatrix}\begin{pmatrix} \nu_L \\ \nu_R^C \end{pmatrix} + h.c. \end{aligned} \tag{1.9}$$

where we have used the identity $\overline{\nu_L^C} m_D \nu_R^C = \overline{\nu_R} m_D \nu_L$.

The values obtained from the diagonalization of the matrix are:

$$m_\pm = \frac{1}{2}\left[m_L + m_R \pm \sqrt{(m_L - m_R)^2 + 4m_D^2}\right] \tag{1.10}$$

Although left-handed Majorana masses m_L are possible in principle, in the SM they are constrained to zero by Higgs mechanism, namely left-handed neutrino takes part in weak interactions with the $W^\pm$ and Z^0 and if they were very heavy the theory would be disturbed (spiegare meglio!!!). On the other hand right handed neutrinos do not take part in weak interactions and so their mass m_R can be large. The heaviness of m_R cannot be motivated in the framework of SM, but if one believes that SM is a theory that describes the world only at low energy scale, it is quite natural to expect that the m_R is generated at ultra-high energy by the symmetry breaking of the theory beyond the SM.

The idea of the simplest version of the See-Saw mechanism, is to assume that the mass term m_L are zero to begin with, but are generated effectively, after right-handed neutrinos are introduced. Another fundamental assumption, as anticipated is that $m_R \gg m_D$. In this hypotesis the eigenvalues of the mass matrix 1.10 are:

$$m_+ \simeq m_R, \quad m_- \simeq \tfrac{m_D^2}{m_R} \tag{1.11}$$

1.4 Neutrino mixing

Once introduced the mass term in the Lagrangian, neutrino vaweform could be described by means of the mass eigenstates (ν_1, ν_2, ν_3) rather than

the flavour eigenstates. Assuming the simpliest description, with three active neutrinos, CPT invariance and no sterile neutrino, the two different bases are related by a unitary 3x3 matrix U, the *lepton mixing matrix* (known as the Pontecorvo-Maki-Nakagawa-Sakata matrix):

$$\begin{pmatrix} \nu_e \\ \nu_\mu \\ \nu_\tau \end{pmatrix} = \begin{pmatrix} U_{e1} & U_{e2} & U_{e3} \\ U_{\mu 1} & U_{\mu 2} & U_{\mu 3} \\ U_{\tau 1} & U_{\tau 2} & U_{\tau 3} \end{pmatrix} \begin{pmatrix} \nu_1 \\ \nu_2 \\ \nu_3 \end{pmatrix} \tag{1.12}$$

This matrix can be parameterized in terms of three mixing angles θ_{ij} and three complex phases (one named after Dirac and the other two after Majorana). Generally, a 3x3 unitary matrix has six phases but, in this case, three of them are removed by properly choosing the eigenstastes. The most common parametrization of the mixing matrix is:

$$\begin{aligned} U = & \begin{pmatrix} 1 & 0 & 0 \\ 0 & c_{23} & s_{23} \\ 0 & -s_{23} & c_{23} \end{pmatrix} \times \begin{pmatrix} c_{13} & 0 & s_{13}e^{-i\delta} \\ 0 & 1 & 0 \\ -s_{13}e^{-i\delta} & 0 & c_{13} \end{pmatrix} \\ & \times \begin{pmatrix} c_{12} & s_{12} & 0 \\ -s_{12} & c_{12} & 0 \\ 0 & 0 & 1 \end{pmatrix} \times \begin{pmatrix} e^{i\alpha_1/2} & 0 & 0 \\ 0 & e^{i\alpha_2/2} & 0 \\ 0 & 0 & 1 \end{pmatrix} \end{aligned} \tag{1.13}$$

where s_{ij} and c_{ij} stand for rispectively, the sines and cosines of the mixing angles θ_{ij}, δ is the Dirac phase and α $(i = 1, 2)$ are the Majorana phases. The matrix U is factorized in a matrix product of four matrices associated with the physics of neutrinos coming from different sources. As will be shown in section 1.6, experiments with three different sources are possible and they investigate different oscillation channels.

Atmospheric neutrinos suggest the possibility of having $\nu_\mu \to \nu_\tau$ oscillation (first matrix). The second matrix is usually associated with the physics of reactor neutrino oscillations ($\nu_e \to \nu_\mu, \nu_\tau$) and here a δ, providing a possible source of CP violation, appears. The third matrix is probed by experiments with Solar neutrinos (commonly interpreted as $\nu_e \to \nu_\mu$ oscillations). The

last matrix contains the Majorana phases that are not involved in neutrino oscillations.

1.5 Neutrino oscillations

The history of neutrino oscillations dates back to the work by Pontecorvo who in 1957 proposed $\nu \to \overline{\nu}$ oscillations in analogy with $K \to \overline{K}$ oscillations [13], described as the mixing of two Majorana neutrinos. Pontecorvo was the first to realise that what we call "electron neutrino", for example, may be a linear combination of mass eigenstate neutrinos, and that this feature could lead to neutrino oscillations such as $\nu_e \to \nu_\mu$. From equation 1.12 we see that if neutrinos have mass, the eigenstate ν_α ($\alpha = e, \mu, \tau$) produced in the weak interaction is, in general, a linear combination of the mass eigenstates ν_i ($i = 1, 2, 3$):

$$|\nu_\alpha\rangle = \sum_{i=1}^{3} U^*_{\alpha i} |\nu_i\rangle \tag{1.14}$$

After travelling for a time t, a neutrino originally produced with flavour α evolves as follows:

$$|\nu_\alpha(t)\rangle = \sum_{i=1}^{3} U^*_{\alpha i} |\nu_i(t)\rangle \tag{1.15}$$

where

$$|\nu_i(t)\rangle = e^{-iE_i t}|\nu_i(0)\rangle \quad \text{and} \quad \mathcal{H}|\nu_i(t)\rangle = E_i|\nu_i(t)\rangle \tag{1.16}$$

At time t the probabilty to find neutrino with flavour β, is given by:

$$P(\nu_\alpha \to \nu_\beta) = |\langle \nu_\beta | \nu_\alpha(t)\rangle|^2 \tag{1.17}$$

$$= \left| \sum_{i=1}^{3} U_{\beta i} e^{-iE_i t} U^*_{\alpha i} \right|^2 \tag{1.18}$$

$$= \sum_{i=1}^{3}\sum_{j=1}^{3} U^*_{\alpha i} U_{\beta i} U_{\alpha j} U^*_{\beta j} e^{-i(E_i - E_j)t} \tag{1.19}$$

For ultrarelativistic neutrinos, the dispersion relation can be approximated by:

$$E_k \simeq E + \frac{m_k^2}{2E} \tag{1.20}$$

Moreover in this condition $t \simeq L$[2]. With this approximation the oscillation probability could be expressed as:

$$\begin{aligned} P(\nu_\alpha \to \nu_\beta) &= \delta_{\alpha\beta} \\ &- 4\sum_{i>j} \Re\left(U^*_{\alpha i}U_{\beta i}U_{\alpha j}U^*_{\beta j}\sin^2\left[1.27\Delta m^2_{ij}\left(L/E\right)\right]\right) \\ &+ 2\sum_{i>j} \Im\left(U^*_{\alpha i}U_{\beta i}U_{\alpha j}U^*_{\beta j}\sin^2\left[2.54\Delta m^2_{ij}\left(L/E\right)\right]\right) \end{aligned} \tag{1.21}$$

where $\Delta m^2_{ij} = m^2_i - m^2_j$ is in eV^2, L in km and E in GeV.

In the simplified scenario of two neutrino mixing ν_α, ν_β, there is only one mass squared difference and the mixing matrix can be parameterized in terms of one mixing angle:

$$U = \begin{pmatrix} \cos\theta & \sin\theta \\ -\sin\theta & \cos\theta \end{pmatrix} \tag{1.22}$$

The resulting transition probability can be written as:

$$P(\nu_\alpha \to \nu_\beta) = \sin^2 2\theta \sin^2\left(1.27\frac{\Delta m^2 L}{E}\right) \tag{1.23}$$

This expression is useful because the results of oscillations experiments are often analysed in first approximation in a two family scenario. An experiment is charaterized by the typical neutrino energy E and by the source-detector distance L. Once these variables are fixed, different values of transition probability are possible depending on Δm^2 and $\sin^2 2\theta$. In order to be sensitive to a given value of Δm^2, an experiment can be optimised choosing $E/L \approx \Delta m^2$. If $E/L \gg \Delta m^2$ the oscillation does not have enough time to

[2] in natural units: $\hbar = c = 1$

yield a detectable effect because $\sin^2(\Delta m^2 L/E) \ll 1$. On the other hand if $E/L \ll \Delta m^2$ it is possible to show that the oscillation phase is smeared out to $\sin^2(\Delta m^2 L/E) = 1/2$ by the finite energy and spatial resolution of the detectors.

When neutrino pass through matter, they undergo coherent forward scattering with particles encountered through their path. This can modify the oscillation probability, which can be enhanced by a resonance under determined conditions (Mikheyev-Smirnov-Wolfenstein effect [17]). Neutrino propagation through matter can be described by the Schrödinger equation with an effective hamiltonian; it is described by a matrix in the neutrino flavour space, which differs, from the corresponding one in the case of vaccum oscillations, by the presence of additional energy terms due to scattering interactions of neutrinos with matter. For electron neutrinos, the additional term is given by:

$$\sqrt{2} G_F N_e \tag{1.24}$$

and comes from ν_e scattering with matter electrons induced by the exchange of the charged boson $W^{\pm}$ (charged current interaction); G_F is the Fermi constant and N_e is the electron density of crossed matter. The same contribution is not present in the hamiltonian for ν_μ and ν_τ, since in ordinary matter the corresponding charged leptons μ and τ are not present, hence scattering due to charged current interaction are not possible. There is a common contribution to the interaction energy due to the neutral current interactions, which is the same for all flavours; therefore, for what concerns oscillations, this contribution translates in a global phase factor and is uneffective. Instead the term coming from equation 1.24 affects the ν_e oscillation probability; this effect is particularly important when neutrino propagates through dense matter like in the Sun.

Source	Type of ν	$\overline{E}[MeV]$	$L[km]$	$\min(\Delta m^2)[eV^2]$
Reactor	$\overline{\nu}_e$	~ 1	1	$\sim 10^{-3}$
Reactor	$\overline{\nu}_e$	~ 1	100	$\sim 10^{-5}$
Accelerator	$\nu_\mu, \overline{\nu}_\mu$	$\sim 10^3$	1	~ 1
Accelerator	$\nu_\mu, \overline{\nu}_\mu$	$\sim 10^3$	1000	$\sim 10^{-3}$
Atmospheric	$\nu_{\mu,e}, \overline{\nu}_{\mu,e}$	$\sim 10^3$	10^4	$\sim 10^{-4}$
Solar	ν_e	~ 1	1.5×10^8	$\sim 10^{11}$

Table 1.1: Sensitivity of different oscillation experiments.

1.6 Experimental results

There are a large number of experiments trying to observe neutrino oscillations. Some rely on man-made sources like nuclear reactors or accelerators; others rely on "natural" sources such as solar neutrinos or neutrinos from cosmic-rays (atmospheric neutrinos). All of these neutrino oscillation experiments are complementary because they involve neutrinos of different energies travelling over different distances, making them sensitive to different Δm^2 as shown in Table 1.1

The detectors are designed to be large in order to compensate the small neutrino interaction cross sections and are often placed underground to shield the cosmic muons. All data on neutrino oscillations collected so far can be analysed in the two flavour effective framework with very good agreement. This can be done, since the measured mass differences show a clearly separeted spectrum, i.e. $\Delta m_\odot = |\Delta m^2_{12}| \ll |\Delta m^2_{13}| \simeq |\Delta m^2_{23}| = \Delta m^2_{atm}$; futhermore, the mixing angle θ_{13} coupling the two oscillations is very small [18, 19, 20]. Therefore, the experimental observations on neutrino oscillations can be divided in two groups, according to the measured parameters:

- experiments on solar and nuclear reactor neutrinos, measuring $\Delta m^2_\odot$ and $\sin^2 2\theta_\odot$;

- experiments on atmosferic and accelerator neutrinos, measuring Δm^2_{atm} and $\sin^2 2\theta_{atm}$;

All the neutrino oscillation experiment did not find indications of a different Δm^2 with respect to $\Delta m^2_{\odot}$ and Δm^2_{atm}, except for the LSND accelerator experiment, which found an appearance signal in the $\overline{\nu}_\mu \rightarrow \overline{\nu}_e$ channel [21], compatible with oscillation hypotesis with a Δm^2 in the 0.1 to 1 eV^2 range. A similar result has been recently reported by the MiniBooNE collaboration [22]. These results should require the existence of at least one additional neutrino type, to account for the observed mass spectrum. This neutrino should be sterile, since, as report in 1.1, precision measurements of Z boson lifetime at LEP show that the number of active neutrino flavours is three[3], hence a fourth neutrino should not have couplings with Z and W bosons. Further study are on-going to fully understand this anomaly;

1.6.1 Solar neutrinos

Solar neutrino experiments are based on the observation of electron neutrinos produced by the Sun, which is an intense source of low energy ν_e by fusion reactions in the pp chain and CNO cycle; the neutrino flux is calculated on the basis of the Standard Solar Model (SSM) [23]. Two types of solar neutrino experiments have been performed: radiochemical experiments (Homestake, Sage, Gallex, GNO) and large Cherenkov experiments (Super-Kamiokande and SNO). The pioneering Homestake experiment opened the "solar neutrino problem" finding nearly 1/3 of the expected ν_e flux from Sun by studying the reaction $\nu_e + {}^{37}Cl \rightarrow {}^{37}Ar + e^-$ [24]. In the '90s SAGE and Gallex/GNO both based on the reaction $\nu_e + {}^{71}Ga \rightarrow {}^{71}Ge + e^-$ observed $\sim$ 71 SNU[4] over the 130 expected [25]. A summary of the results obtained by radiochemical solar-neutrino experiments is shown in Table 1.2

Super-Kamiokande studied, using water to detect the Cherenkov light emitted, two channels, the charged current interactions (CC) of electron

[3] assuming that their masses are smaller than $\sim 45\ GeV$

[4] Solar Neutrino Units = 10^{-36} captures per second per absorber nucleus

	$^{37}Cl \rightarrow^{37} Ar$ (SNU)	$^{71}Ga \rightarrow^{71} Ge$ (SNU)
Homestake	$2.56 \pm 0.16 \pm 0.16$	-
GALLEX	-	$77.5 \pm 6.2^{+4.3}_{-4.7}$
GNO	-	$62.9^{+5.5}_{-5.3} \pm 2.5$
CNO + GALLEX	-	$69.3 \pm 4.1 \pm 3.6$
SAGE	-	$65.4^{+3.1+2.6}_{-3.0-2.8}$
SSM	$8.46^{+0.87}_{-0.88}$	$127.9^{+8.1}_{-8.2}$

Table 1.2: Results from radiochemical solar-neutrino experiments.

neutrino with the electrons of the detector performed by the exchange of W^- and the neutral current interaction (NC) mediated by Z^0 which can be performed by neutrino of all flavour [26]. The detection of Cherenkov light allowed, unlike previous experiment, a real-time and directional study of the events collected in the detector, allowing a reliable tagging of solar neutrino events. It was mainly sensitive to ν_e because the CC cross-section is larger and, even though it had some sensitivity to NC, a significant deficit in the expected solar neutrino flux was observed.

The SNO (Sudbury Neutrino Observatory) detector used a heavy water (D_2O) target 2.5 km underground surrounded by photomultipliers in order to detect the Cherenkov light produced by particles originated in three reactions: CC interactions $\nu_e d \rightarrow ppe^-$, NC interactions $\nu_x d \rightarrow pn\nu_x$, where ν_x can be any of the three flavours, and elastic scattering (ES) interaction $\nu_x e^- \rightarrow \nu_x e^-$. The CC reaction is sensitive only to ν_e, while the NC reaction is equally sensite to all active neutrino flavours ($x = e, \mu, \tau$), this allowed SNO to determine the electron and non-electron neutrino components of the solar neutrino flux, as shown in Fig. 1.1. The measured ν_e was $\sim 1/3$ of the expected [27] and $\Psi_{\nu_e} + \Psi_{\nu_\mu + \nu_\tau}$ was as expected from SSM [28] thus leading to the confirmation of the electronic neutrino oscillation in the other neutrino flavours.

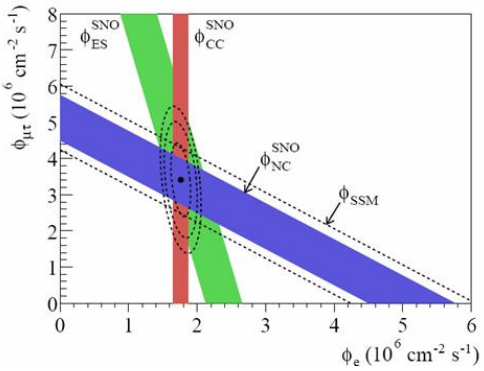

Figure 1.1: Fluxes of ^8B solar neutrinos, Ψ_{ν_e}, and $\Psi_{\nu_\mu+\nu_\tau}$, deduced from the SNO's CC, ES, NC results and from Super-Kamiokande ES results. The SSM prediction is also shown. The bands represent the 1σ error. The contours show the 68%, 95%, 99% joint probability for Ψ_{ν_e} and $\Psi_{\nu_\mu+\nu_\tau}$.

1.6.2 Atmospheric neutrinos

Atmospheric neutrinos are produced in the decay of secondary particles, mainly pions and kaons, created in the interactions of primary cosmic rays with the nuclei of the Earth's atmosphere. Pions and Kaons decay mainly into ν_μ and μ, the latter afterwards decays into e, ν_e and ν_μ. Although the absolute neutrino flux is rather badly known (predictions from different calculations disagree by $\simeq$ 20%), the ratio R of the numbers of muon to electron neutrinos is known at $\simeq$ 5 %:

$$R = \frac{N_{\nu_\mu} + N_{\overline{\nu}_\mu}}{N_{\nu_e} + N_{\overline{\nu}_e}} \simeq 2 \tag{1.25}$$

Neutrino oscillations could manifest as discrepancy between the measured and the expected value of the ratio R. Atmospheric neutrinos are observed through high-energy CC interactions in which the flavour, direction and energy of the incoming neutrino are strongly correlated with the measured flavour, direction and energy of the produced charged lepton. Since neutrinos are penetrating particles, due to their extremely low cross-section, a detector can observe both neutrinos produced in the atmosphere above it and neutrinos coming from the opposite emisphere. The first ones (downwardgo-

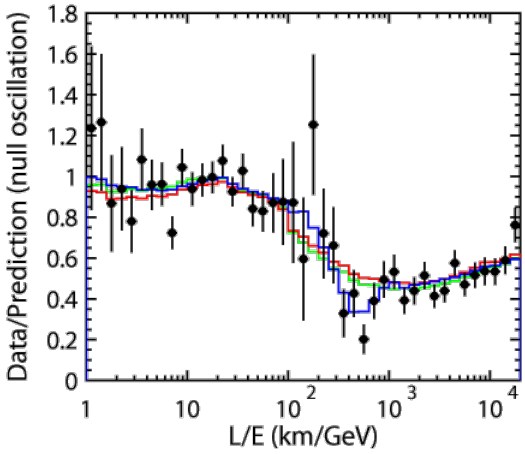

Figure 1.2: Results of the L/E analysis of SK-I atmospheric neutrino data. The points show ratio of the data to the Monte Carlo prediction without oscillations, as a function of the reconstructed L/E.

ing ν) travel a distance of few km, while, for the second ones (upward-going ν), the travelled distance is $\sim$ 10000 km. The cosmic ray flux is isotropic, hence the fluxes of upward-going and downward-going neutrinos of a given flavour should be the same. The Kamiokande-II [29], Super-Kamiokande [30], Soudan-2 [31] and MACRO [32] detectors reported energy dependent deficits in the ν_μ fluxes with respects to the predictions and a distortion of the angular distributions. The Super-Kamiokande experiment observed a convincing evidence of an up/down asymmetry on the ν_μ flux and a deficit for the up-going ν_μ was found as shown in Fig. 1.2.

Since the ν_e data were in agreement with the expectations, the observed deficit could be explained in terms of $\nu_\mu \rightarrow \nu_\tau$ oscillations with maximal mixing and $\Delta m^2_{atm} \sim 2 \cdot 10^{-3} eV^2$. The experiments results are summarized in Table 1.3.

1.6.3 Nuclear reactor experiments

Nuclear reactors produce $\overline{\nu}_e$ with energy of the order of a few MeV. Due to the low energy, electrons are the only charged leptons that can be

Experiment	R
Soudan-2	$0.68 \pm 0.11_{stat} \pm 0.06_{sys}$
MACRO	$0.74 \pm 0.036_{stat} \pm 0.046_{sys} \pm 0.13_{theo}$ $-1.0 < \cos\theta_{zenith} < -0.1$
SK	$R_{sub-GeV} = 0.658 \pm 0.016_{stat} \pm 0.032_{sys}$ $R_{muti-GeV} = 0.702 \pm 0.031_{stat} \pm 0.099_{sys}$

Table 1.3: Results of the atmospheric neutrino experiments

produced in neutrino CC interactions. If $\overline{\nu}_e$ oscillates to another flavor, its CC interaction cannot not be observed because the neutrino has not enough energy in the laboratory frame to produce the associated charged lepton. Therefore oscillation experiments performed at reactors are disappearance experiments. They have the advantage that smaller value of Δm^2 can be accessed due to the lower neutrino energy. Reactor neutrino experiments can test either solar or atmospheric oscillations, they measure the survival probability $P(\overline{\nu}_e \rightarrow \overline{\nu}_e)$ of the electrons antineutrinos emitted by fission reactions in the reactor and travelling for a distance L: for L of the order of about few tens of kilometers the solar region can be studied, for distances that don't exceed few kilometers the parameters of the atmospheric oscillation are involved. If $\Delta m^2_{\odot} \ll \Delta m^2_{atm}$ and/or θ_{13} is small enough, as it is the case, the solar driven and the atmospheric driven oscillations decouple to a first approximation in the oscillation probability formula $1 - P(\overline{\nu}_e \rightarrow \overline{\nu}_e)$.

Two experiment were performed to study the parameter region of the atmospheric neutrino oscillations: the CHOOZ experiment [18] was located 1050 m away from the Chooz two-reactor nuclear power plant in France, while the Palo Verde experiment [19] used a segmented detector 750 and 890 m away from a three-reactors nuclear power plants in Arizona. Both experiments measured a $\overline{\nu}_e$ flux in agreement with expectations and thus excluded any $\overline{\nu}_e \rightarrow \overline{\nu}_\mu, \overline{\nu}_\tau$ oscillation in the Δm^2_{atm} region; the CHOOZ experiment also provided the best constrint on the upper limit of the θ_{13} mixing angle.

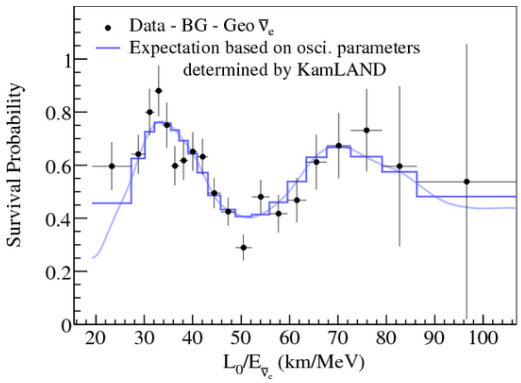

Figure 1.3: The ratio of the background and geoneutrino-subtracted $\overline{\nu}_e$ spectrum to the prediction one without oscillation as function of L_0/E, where $L_0 = 180\ km$.

The KamLAND experiment [33] located in the Kamioka mine in Japan 180 km away on average from the source sensitive to $\Delta m^2_{\odot}$ studied $\overline{\nu}_e$ disappearance, it reproduced solar neutrino oscillations on Earth (see Fig. 1.3) and contributed to the measurement of oscillation parameters, in particular of the $\Delta m^2_{\odot}$ value. The solutions found by KamLAND and by the solar experiment agree and the allowed domains in the parameters space largely overlap. By combining KamLAND with the solar neutrino experiment, it is possible to remove ambiguities and estimate two oscillation parameters:

$$\sin^2 2\theta_{\odot} = 0.3141^{+0.18}_{-0.15} \quad (1.26)$$

$$\Delta m^2_{\odot} = (7.921 \pm 0.09) \times 10^{-5} eV^2 \quad (1.27)$$

1.6.4 Accelerator experiments

Beams of muons meutrinos can be produced at accelerators allowing *Long Baseline* and *Short Baseline* experiments (depending on the neutrino travelled distance) to study the atmospheric neutrino oscillation. These experiments can look for disappearance of the beam neutrino or for appearance of a different neutrino flavour in the beam (*disappearance* and *appearance* experi-

ments). The ratio L/E should be the best to reach the oscillation maximum, apart in the special case of τ appearance where this is not compatible with the τ production cross section which requires a high energy beam, in this case the number of τ produced is maximized.

The K2K (KEK-to-Kamioka) long-baseline neutrino oscillation experiment is the first accelerator-based experiment with a neutrino path lenght extending hundred kilometers. A pulsed muon neutrino beam pure at 98%, with a mean energy $E \sim 1.3\ GeV$ was produced by an accelarator and directed to the Super-Kamiokande at a distance of 250 km. The spectrum and the profile of the neutrino beam were measured by a near neutrino detector, similar to SK, in order to estimate the interactions expected in the far detector and to reduce the systematics in the comparison. Super-Kamiokande events caused by accelerator-produced neutrinos were selected using the timing information from the global positioning system. The number of beam-originated events observed by Super-Kamiokande was 112, compared with an expectation of $158.1^{+9.2}_{-8.6}$ events without oscillation. Furthermore, the neutrino energy was reconstructed for 58 events and the measured spectrum showed the distortion expected from neutrino oscillations. The oscillation parameters determined by K2K are compatible with that measured with atmospheric neutrino data and their best-fit is:

$$\Delta m^2_{atm} = 2.8 \times 10^{-3} eV^2 \tag{1.28}$$

$$\sin^2 2\theta_{atm} = 1 \tag{1.29}$$

Long-baseline experiments which are now taking data are the MINOS experiment in the USA, the T2K (Tokai ti Kamioka) experiment in Japan and OPERA in Europe.

T2K uses the Super-Kamiokande detector and neutrinos travel a distance of $L \sim 300\ km$ in order to test the ν_e appearance in the ν_μ beam produced at the J-Parc PS in Japan. T2K is the first experiment that exploits an "off-axis" beam. In this way the energy spectrum of the neutrino beam

seen by the Super-Kamiokande detector is very peaked around the oscillation maximum ($L/\langle E\rangle \sim 500\ km/GeV$) with attenuated high energy tail. In 2011 it observes indications of $\nu_\mu \to \nu_e$ appearance, observing, after kinematical and topological cuts, 6 electron-like events while they expected 1.5 ± 0.3 events, assuming $\sin^2\theta_{13} = 0$. This result converted into a confidence interval yields $0.03 < \sin^2\theta_{13} < 0.28$ at $90\% C.L.$ for $\sin^2\theta_{23} = 1.0$, $|\Delta m^2_{23}| = 2.4 \times 10^{-3} eV^2$ and $\delta_{CP} = 0$.

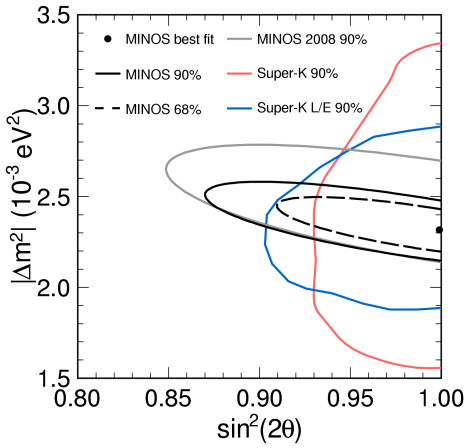

Figure 1.4: Confidence interval contours in the fit of the MINOS Far Detector data to the hypotesis of two flavour oscillations.

MINOS is the second long-baseline neutrino oscillation experiment with near and far detector; both the detectors are iron-scintillator tracking calorimeters with toroidal magnetic field. The near detector has a mass of 0.98 *kton*; the far detector has a mass of 5.4 *kton* and it is placed at 735 *km* from the neutrino source. Muon neutrinos are produced by the NuMI facility using 120 *GeV* protons from the Fermilab Main Injector; the neutrino energy spectrum can be varied by moving the target position relative to the magnetic focusing system, moreover horn and corn magnetic field polarity can be inverted, allowing the study of $\overline{\nu}_\mu$ disappearance. In 2011 MINOS was able to improve the measurement of the value of the atmospheric mass splitting and

of the mixing angle, rispectively:

$$|\Delta m^2| = (2.32^{+0.12}_{-0.08}) \times 10^{-3} eV^2 \tag{1.30}$$

$$\sin^2 2\theta > 0.90 \quad (90\% C.L.) \tag{1.31}$$

This result (Fig. 1.4) is the most precise measurement of this mass splitting to date.

The Opera experimentis as well a long-baseline appearance experiment designed to prove the $\nu_\mu \rightarrow \nu_\tau$ oscillation in the neutrino beam produced at CERN by detecting ν_τ interactions 730 km away from the source.

1.7 The global oscillation picture

It is to be noticed that neutrino oscillations do not give information about the sign of the neutrino mass squared differences, so there are two possible ordering schemes for neutrino masses that are consistent with the explanation of the atmospheric and solar result of neutrino oscillations: the *normal* and *inverse* hierarchies. By definition the m_1 is lighter than m_2, so the normal hierarchy is the one for which the third neutrino mass eigenvalue m_3 is bigger than the others, while the inverse one is that for which m_3 is the lightest mass eigenvalue. The best world estimates on neutrino masses and mixing from oscillation data are summarized in Table 1.4

Parameter	Best fit $\pm$ 1σ	2σ	3σ
Δm^2_{21} $[10^{-5} eV^2]$	$7.59^{+0.20}_{-0.18}$	7.24 - 7.99	7.09 - 8.19
Δm^2_{31} $[10^{-3} eV^2]$	2.45 ± 0.09	2.28 - 2.64	2.18 - 2.73
	-$(2.34^{+0.10}_{-0.09})$	-(2.17 - 2.54)	-(2.08 - 2.64)
$\sin^2\theta_{12}$	$0.312^{+0.017}_{-0.015}$	0.28 - 0.35	0.27 - 0.36
$\sin^2\theta_{23}$	0.51 ± 0.06	0.41 - 0.61	0.39 - 0.64
	0.52 ± 0.06	0.42 - 0.61	0.39 - 0.64
$\sin^2\theta_{13}$	$0.010^{+0.009}_{-0.006}$	≤ 0.027	≤ 0.035
	$0.013^{+0.009}_{-0.007}$	≤ 0.031	≤ 0.039

Table 1.4: A summary of neutrino oscillation parameters. For Δm^2_{31}, $\sin^2\theta_{23}$ and $\sin^2\theta_{13}$ the upper (lower) row corresponds to normal (inverted) neutrino mass hierarchy.

It has to be noticed that recently two main anomaly in the neutrino scenario arise: the so called "Gallium anomaly" and the "reactor $\overline{\nu}$ anomaly". Gallium anomaly concerns Gallium solar experiment, for which the $\nu + Ga$ cross section value has been measured by a test experiment performed on SAGE detector from April to September 2004, in order to verify the well understanding of the detector efficiencies. The test experiment measured a Ge production rate which is about 0.79% of the theoretically calculated production rate, leading to an indication that the theoretical cross section, used in the evaluation of the expection rate due solar neutrino in the gallium solar experiment, has been overestimated. This leads to an indication of short-baseline electron neutrino disappearance that could be interpreted as $\nu_e \rightarrow \nu_s$ oscillation with $sin^2\theta \gtrsim 0.07$ and $\Delta m^2 \gtrsim 0.35\ eV^2$ at 99%C.L.. Reactor $\overline{\nu}$ anomaly is related to a new expected reactor $\overline{\nu}$ spectra for ^{235}U, ^{239}Pu, ^{241}Pu and ^{238}U, which increases the mean $\overline{\nu}$ flux by about 3%. To a good approximation, this reevaluation applies to all reactor neutrino experiments and in particular for experiments with reactor-detector distances $< 100\ m$, for which, with the new flux evaluation, tha ratio of the observed

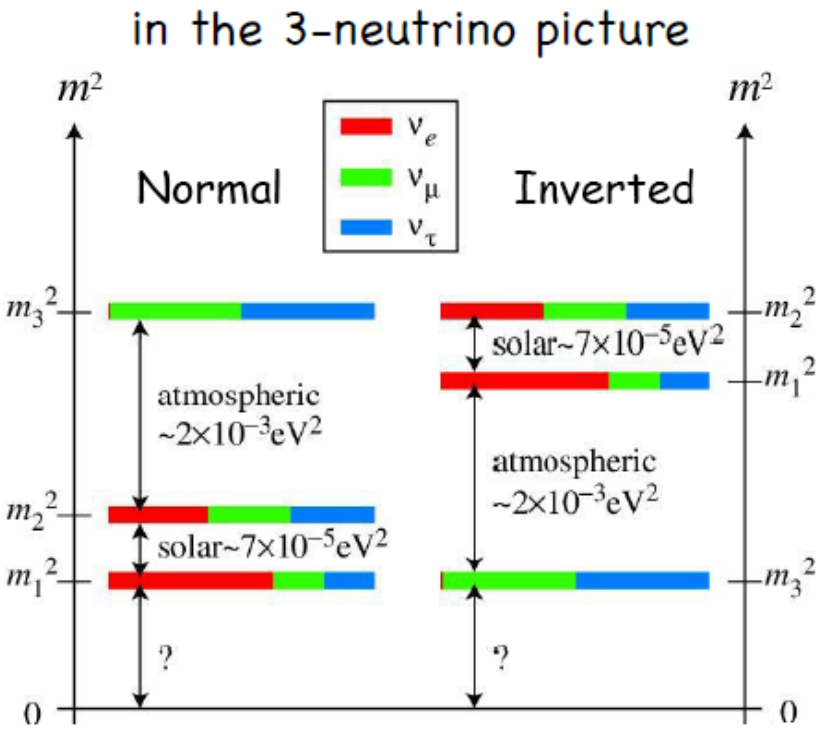

Figure 1.5: Alternative neutrino mass patterns that are consistent with neutrino oscillation explanation of the atmospheric and solar data. The coloured bands represents the value of the mixing between mass eigenstates and weak eigenstates, i.e. $|U_{\alpha i}|^2$.

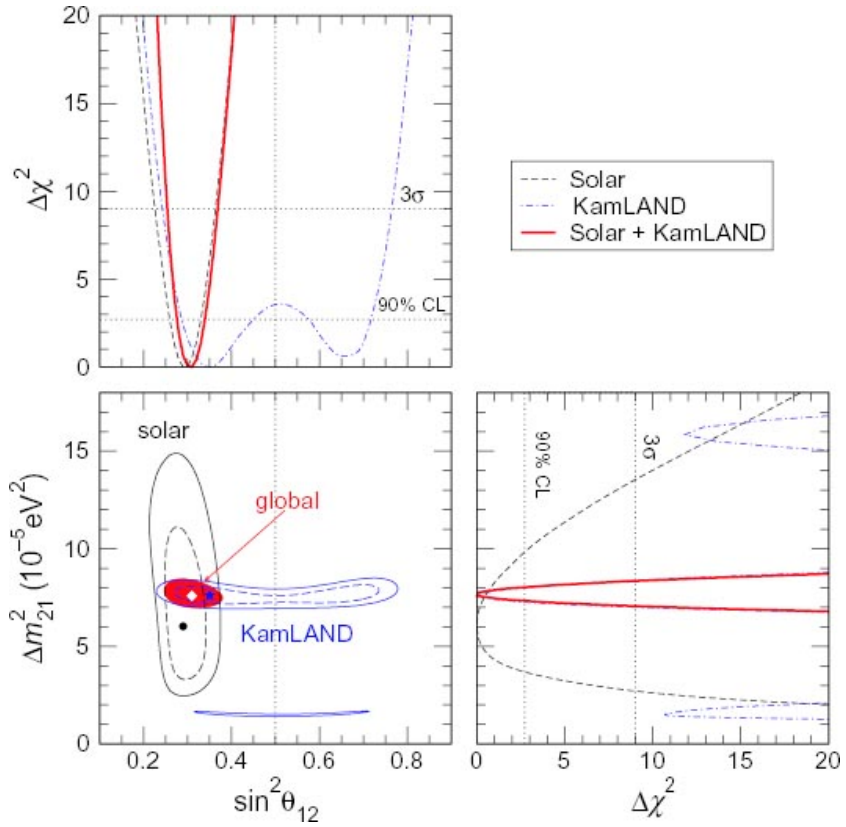

Figure 1.6: Determination of the leading solar oscillation parameters from the interplay of data from artificial and natural neutrino sources. χ^2 profiles and allowed regions at 90 and 99.73% confidence level (CL) (2 degrees of freedom (d.o.f.)) for solar and KamLAND, as well as 99.73% CL region for the combined analysis are shown. The dot, star and diamond, indicate the best fit points of solar data, KamLAND and global data, respectively.

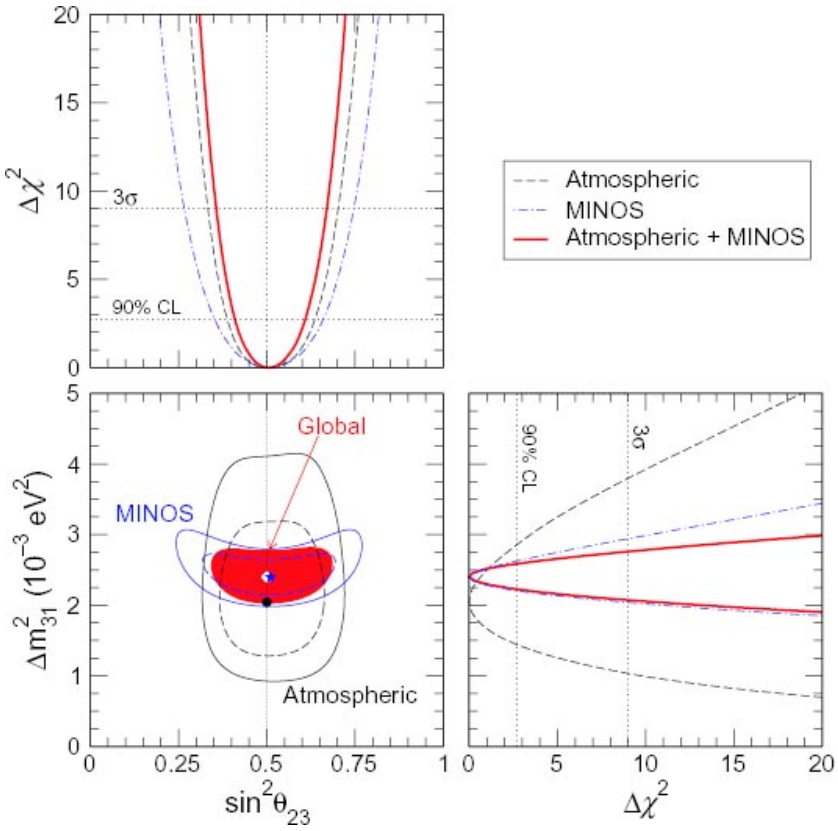

Figure 1.7: Determination of the leading atmospheric oscillation parameters from the interplay of data from artificial and natural neutrino sources. χ^2 profiles and allowed regions at 90 and 99.73% (CL) (2 d.o.f.) for atmospheric and MINOS, as well as 99.73% CL region for the combined analysis (including also K2K) are shown. The dot, star and diamond, indicate the best fit points of atmospheric data, MINOS and global data, respectively.

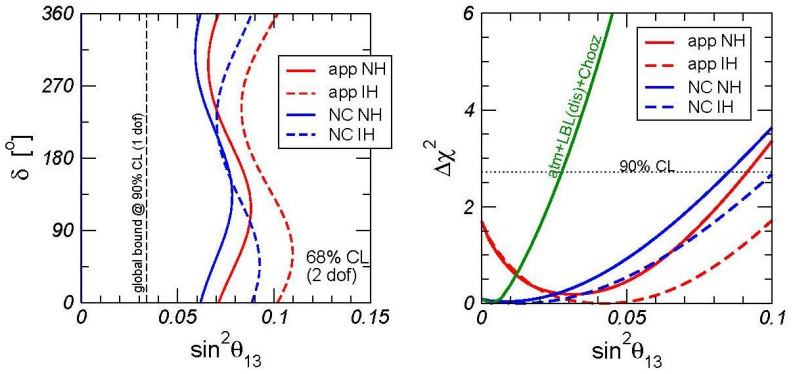

Figure 1.8: Left: Allowed regions in the ($sin^2\theta_{13}$ - δ) plane at 68% C.L. (2 d.o.f.) for MINOS ν_e appearance and NC data. Regions are shown separately for normal (NH) and inverted (IH) neutrino mass hierarchy. For comparison we show also the bound from global data at 90% C.L. (1 d.o.f.). Right: $\Delta\chi^2$ projection as a function of $sin^2\theta_{13}$ for MINOS ν_e appearance and NC data, assuming NH (solid) and IH (dashed), both with respect to the common minimum, which occurs for IH. The green solid curve corresponds to the bound from CHOOZ, atmospheric, K2K and MINOS (disappearance) data.

event rate to predicted rate becomes 0.943 ± 0.023, leading to a deviation from unity at 98.6% C.L. that can be interpreted as new neutrino oscillation, such that $|\Delta m^2_{new}| > 1.5\ eV^2$ and $sin^2(2\theta_{new}) = 0.14 \pm 0.08$ at 95% C.L..

For what concerns θ_{13} a global analysis of the oscillation data [35], including the recent results obtained by T2K and MINOS (reported in 1.6.4), lead to a best $sin^2\theta_{13}$ value:

$$sin^2\theta_{13} = \begin{cases} 0.021 \pm 0.007, & \text{old reactor fluxes} \\ 0.025 \pm 0.007, & \text{new reactor fluxes} \end{cases} (1\sigma), \tag{1.32}$$

corrisponding to a $> 3sigma$ evidence in favor of nonzero θ_{13}. It is to be noticed that in the global fit of [35], the CP-violation parameter δ is not a free parameter, so a clear evidence could be strenghtened only removing this limitation.

Chapter 2

Opera Experiment

OPERA (Oscillation Project with Emulsion-tRacking Apparatus) is a long baseline neutrino experiment aiming at the observation of direct ν_τ appearance in a pure ν_μ beam. This would represent the final and unambiguous proof of the $\nu_\mu \leftrightarrow \nu_\tau$ oscillation as it has been interpreted in the atmospheric sector by disappearance experiments like Super-Kamiokande, MACRO and MINOS.

The direct appearance search is based on the detection of τ leptons produced in the charged current interactions (CC) of τ neutrinos. The neutrino beam is produced by the protons accelerated in the CERN SPS and injected in the CNGS beam line, 730 km away from the detector location. The OPERA experiment is installed in Hall C of the underground Gran Sasso Laboratory (LNGS), aligned with the CNGS baseline, under 1400 meters of rock overburden.

The experiment was designed to identify the tau lepton, characterized by a very short lifetime ($c\tau = 87\mu m$) according to its decay topology and kinematics. This requires a micrometric resolution and a mass of the order of a $kton$, to maximize the neutrino interaction probability.

To fulfill these requirements, the detector concept is based on the Emulsion Cloud Chamber (ECC) technique, combined with real-time detection techniques (electronic detectors): OPERA is a hybrid apparatus with a mod-

ular structure. The ECC basic unit in OPERA is a brick made of 56 lead plates (absorbers), providing the necessary mass, interleaved with 57 nuclear emulsion films, providing the necessary spatial and angular resolution. The electronic detectors are used to trigger the neutrino interactions, to locate the brick in which the interaction took place, to identify muons and measure particle momentum and charge. The analysis of the emulsion is performed in the OPERA laboratories all over the world by automatic scanning systems developed to measure the large ammount of emulsion involved in the experiment.

2.1 The CNGS Beam

The CNGS beam was designed and optimized for the ν_τ appearance starting from a pure ν_μ beam. The high energy of the beam (the mean neutrino energy is $\sim 17\ GeV$), well above the threshold for τ production, was chosen to maximize the number of CC interactions at Gran Sasso of ν_τ produced by the oscillation mechanism. The average L/E_ν ratio is 43 km/GeV, that makes the ν_μ spectrum "off peak" with respect to the maximum oscillation probability for $\Delta m^2 = 2.4 \times 10^{-3}\ eV^2$: this choise comes from a compromise between the requirements of a significant CC interaction cross section and a large oscillation probability.

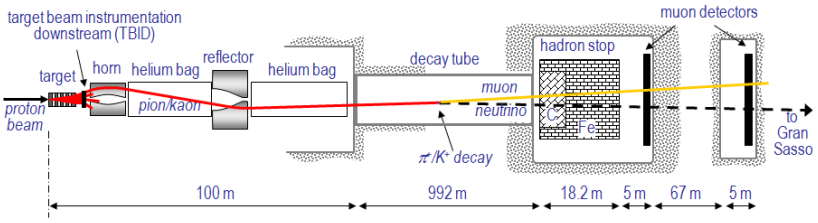

Figure 2.1: Schematic outline of the main component of the CNGS beam line

The CNGS is a conventional neutrino beam: the 400 GeV/c proton beam extracted from the SPS accelerator hits a carbon target producing pions and

$L/\langle E_{\nu_\mu}\rangle$	43 (km/GeV)
ν_μ	$7.36 \times 10^{-9}(m^{-2}pot^{-1})$
ν_e/ν_μ	0.89%
$\overline{\nu}_e/\nu_\mu$	0.06%
$\overline{\nu}_\mu/\nu_\mu$	2.1 % (CC)
ν_τ/ν_μ	negligible
$\nu_\mu CC$	$5.05 \times 10^{-17}(pot^{-1}kton^{-1})$

Table 2.1: CNGS beam features and interactions expected in OPERA

kaons. The target unit contains 13 graphite rods with a diameter of 4 mm, well containing the proton beam, for an overall target length of 2 m. The positively charged π/K are energy-selected and focused with two magnetic lenses, called "horn" and "reflector", in the direction of Gran Sasso. Each toroidal lense is 7 m long, and it is followed by a helium tube 31 m long, in order to reduce the interaction probability for secondary hadrons.

After the second helium tube it is located the decay tunnel, 994 m long, with a diameter of 2.45 m, under vacuum at less than 1 $mbar$. Here the focused hadrons form a parallel beam and they decay into ν_μ and μ with an opening angle of $\sim$ 2 $mrad$. All the remaining hadrons, i.e. protons that have not interacted in the target, pions and kaons not decayed in flight, are absorbed by a massive iron and graphite hadron stopper at the end of the vacuum pipe.

The muons, absorbed downstream in around 500 m of rock, are monitored by two muon detector stations. The first one is located immediately downstream to the hadron stopper, the second one after 67 m of rock. This allows to monitor the intensity of the produced neutrino beam and the beam profile, giving an on-line feedback of the beam quality. The separation of the two stations allows a rough estimation of the muon energy spectrum, since the energy threshold is different in the two chambers.

During a nominal cycle there are two SPS extractions separeted by 50

ms, each one lasts 10.5 μs and contains 2.4 $\times$ 10^{13} protons at 400 GeV/c. The CNGS beam features are given in Table 2.1 the $\overline{\nu}_\mu$ contamination is 2.1% in terms of CC interactions, the $(\nu_e + \overline{\nu}_e)$ contamination is lower than 1% and the prompt ν_τ contamination is totally negligible. Due to the Earth curvature, neutrinos from CERN enter the Hall C with an angle of 3.3° with respect to the horizontal plane. The nominal integrated beam intensity is 4.5 $\times$ 10^{19} protons on target (p.o.t.) per year (200 operational days), designed to operate for 5 years. The number of corresponding CC and NC ν_μ interactions expected at Gran Sasso is about 3800/kton/year. Assuming $\Delta m^2 = 2.4 \times 10^{-3} eV^2$ and maximal mixing, at the nominal beam intensity and with a target mass of 1.25 $kton$, 115 ν_τ CC interactions are expected after 5 years of data taking. Considering the overall efficiency to detect the τ, OPERA should observe about 10 signal events with less than one background event.

2.2 The Opera detector

The detector is composed of two identical parts, called supermodules (SM1 and SM2), each consisting of a target section followed by a magnetic spectrometer. In the target, the bricks are arranged in 29 vertical planar structures ("walls"), transverse to the beam direction, interleaved with Target Tracker (TT) walls. Each TT wall consists of a double layered plane of long scintillator strips. The TTs trigger the data acquisition and locate the brick in which the interaction occurred.

The target section is followed by a magnetic spectrometer, a large dipolar iron magnet instrumented with Resistive Plate Chambers (RPC). The magnetic field intensity is 1.53 T, directed along the vertical axis, transverse to the neutrino beam axis. The RPC planes are inserted between the iron slabs to provide tracking capability inside the magnet and the range measurement for stopping muons. The detection of charged particles in the magnet is measured by six stations of vertical drift tubes, the Precision Trackers (PT).

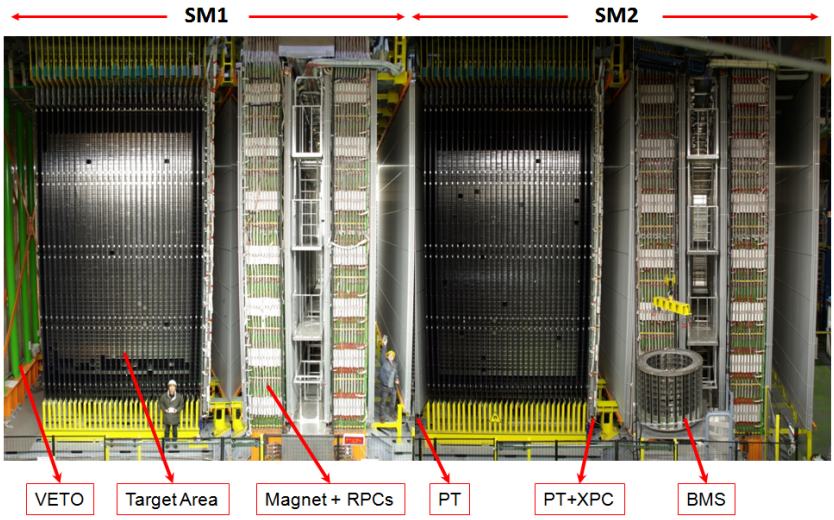

Figure 2.2: View of the OPERA detector. The red horizontal lines at the top indicate the position of the two identical supermodules (SM1 and SM2). Arrows show the position of the VETO planes, the "target area" (ECC brick interleaved with planes of plastic scintillators), the drift tubes (PT) and the XPC, the magnets and the RPC installed between the magnet iron slabs. The Brick Manipulator System (BMS) is also visible.

In order to remove ambiguities in the reconstruction of particle trajectories, each spectrometer is instrumented with additional RPCs with two crossed strip planes tilted with respect to the horizontal and vertical planes, called XPC.

Two glass RPC layers (VETO) are placed in front of the detector, acting as a veto for charged particles originating from the upstream material (mainly muons from interactions in the rock or in the Borexino experiment).

The OPERA detector, shown in Fig 2.2, has a length of 20 m (z coordinate), is 10 m high (y coordinate) and 10 m wide (x coordinate), for a total weight of about 4 $kton$. Each sub-detector and its purpose will be described in more details in the following sections.

2.2.1 Target Tracker

Each brick wall is followed by a Target Tracker (TT) wall. The TT provides realtime detection of the outgoing charged particles, giving "time resolution" to the ECC. Its main task is to locate the brick in which the neutrino interaction took place and to provide calorimetric measurement of the hadronic shower energy.

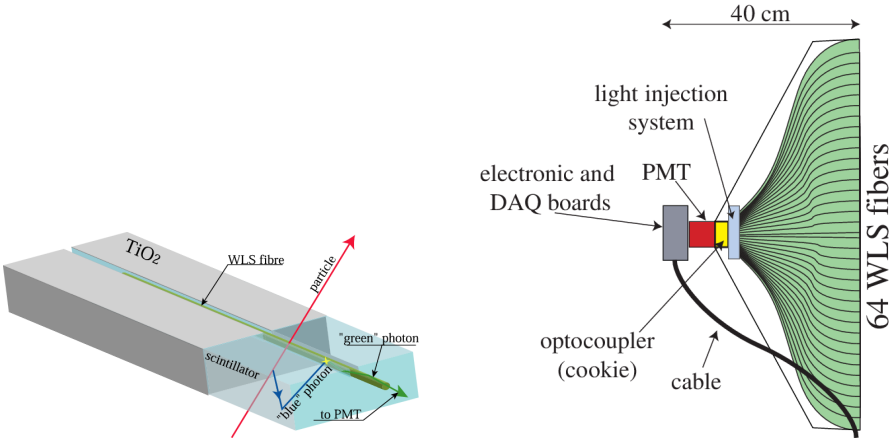

Figure 2.3: Schematic view of a scintillator strip with the WLS (left) and of a strip module end-cap with the front-end electronics and DAQ board (right).

A TT wall consists of two scintillator planes providing the vertical and the horizontal coordinates. Each plane is composed by 256 plastic scintillator strips 6.86 m long, thus covering the 6.7×6.7 m^2 surface defined by the brick wall, with a cross section of 2.63×1.06 cm^2. Along the strip, a 1 mm diameter Wavelength Shifting fiber (WLS) is read on both sides by a multi-anode photomultiplier (PMT), giving a position resolution of ~ 1 cm (Fig. 2.3). The strips are grouped in four modules, each module is read out with a 64-channel Hamamatsu PMT; 16 PMTs per TT wall are used, as shown in Fig. 2.4. With the chosen threshold, equivalent to 1/3 photo-electrons, the mean strip effciency is higher than 99%.

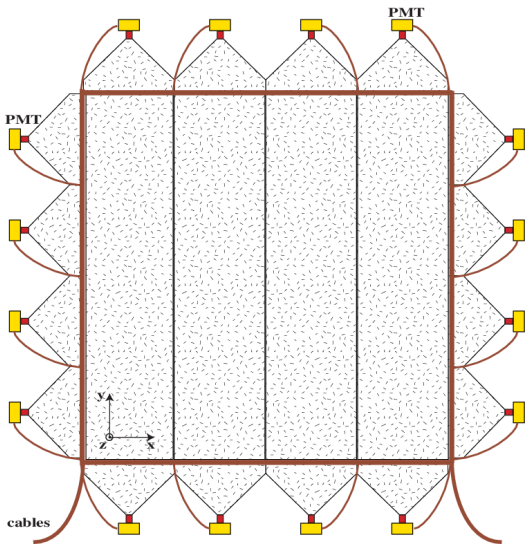

Figure 2.4: Schematic view of a TT wall, formed by one horizontal and one vertical plane. The scintillator strips are grouped in four modules in each plane.

2.2.2 Spettrometer

Magnet

Each of the two dipolar magnets is made of two vertical walls (arms), connected by a top and a bottom flux return yoke (Fig. 2.5). The walls

consist of twelve iron layers 5 *cm* thick, interleaved with RPC planes (Inner Tracker). The geometry of the OPERA magnets has two advantages with respect e.g. to toroidal geometries. The magnetic field along the arms is much more uniform than in a toroid and it is essentially 1-dim., i.e. the components orthogonal to the vertical directions are nearly zero ($B \equiv |\mathbf{B}| \simeq B_y$). The magnets operate at a current of 1600 A, producing a magnetic field essentially uniform with an average flux density of $\sim 1.53\ T$. The field lines are vertical and of opposite orientations in the two magnet arms, where B remains constant within 4%. The transverse size of the dipolar magnet is $10 \times 8.2\ m^2$, the length is 2.64 m, for an overall weight of 990 *ton*.

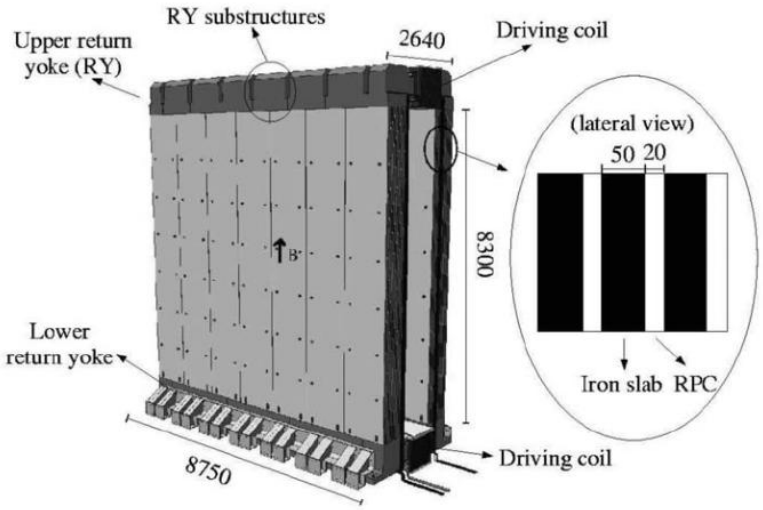

Figure 2.5: Three dimensional view of one OPERA magnet. Units are in *mm*. The blow-up insert shows the dimensions of three of the twelve layers of an arm.

RPC tracking system

Resistive Plate Chamber (RPC) planes are inserted in the 2 *cm* gaps between the iron slabs of the magnet arms (Inner Tracker), in order to reconstruct tracks inside the magnet and to give calorimetric measurements in

combination with the TT . The Inner Trackers are used also to measure the momentum from the range of stopping muons, and to provide the trigger for the Precision Trackers. Each plane is composed of 3×7 RPCs of 2.91×1.134 m^2 surface covering a 70 m^2 area. Each RPC consists of two electrodes, made of two parallel 2 mm thick bakelite planes kept 2 mm apart; the external surface of the electrodes is painted with graphite and protected with PET insulating films (Fig. 2.6). The 2-D read-out is performed by means of 2.6 cm pitch and 8 m long vertical strips (x coordinate), measuring the coordinate in the bending plane, and 3.5 cm pitch and 8.7 m long horizontal strips (y coordinate). The RPCs are operate in streamer mode at the voltage of 5.7 kV with a current of less than 100 nA/m^2. Charged particles crossing the RPC ionize the gas mixture (based on Argon) producing ions and electrons that are drifted in the electric field to the corresponding plate and induce a signal in the copper strips. RPC layer's typical efficiency is about 95%. The time resolution is 4 ns, while the dead time is 10 ms, still suitable for the low event rate in OPERA. A dedicated trigger board allows for the definition of special triggering conditions between the 11 RPC planes of each spectrometer arm and an external validation signal.

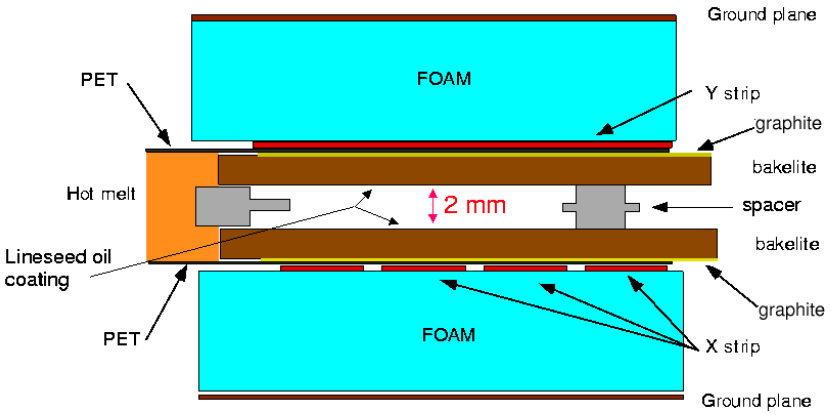

Figure 2.6: Cross-section of a Resisitve Plate Chamber with its associated strips for the read-out of the induced signal.

The XPCs are two RPC planes placed outside the iron magnet, downstream of the target section, with the readout strips inclined by $\pm$ 42.6°C

with respect to the horizontal. Both XPC planes are made of 21 RPCs with a pitch of 2.6 *cm* in each readout direction. The XPCs help in resolving ambiguities in particle reconstruction inside the PTs and contribute with the RPC in the calorimetric measurement of hadronic showers. In addition to the read-out electronics, the XPC and seven RPC layers in each spectrometer are instrumented with dedicated timing boards (TB) used to trigger the Precision Trackers and to give a common stop to their TDCs.

Precision tracker

The Precision Tracker (PT) is used together with the other parts of the muon spectrometer for muon identification, charge determination and momentum measurement. Muons are deflected by the two magnet arms with opposite field direction, forming an S-shaped trajectory: only one track coordinate (x coordinate) has to be measured precisely. The PT measures the muon track coordinates in the bending plane with high precision. It is made of vertical drift tubes arranged in 12 chambers (PT stations), each covering an area $8 \times 8\ m^2$.

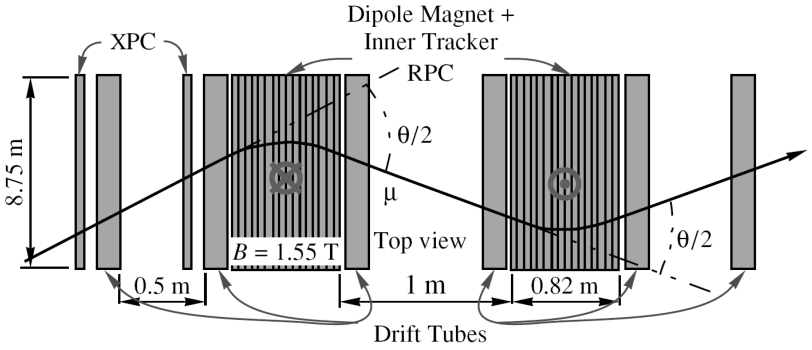

Figure 2.7: Top view of one muon spectrometer (x-z plane), showing the PT and the dipole magnet instrumented with RPC layers (2×11). The drift tube stations are grouped in 3 pairs per magnet arm.

In each SM there are 6 PT stations grouped in 3 pairs. A first couple of consecutive PT stations is placed between the target section and the mag-

net, a second couple is put between the magnet arms and the third couple is located downstream of the magnet (Fig. 2.7). Each drift tube is 8 m long, with 38 mm outer diameter, 0.85 mm wall thickness and a gold-plated tungsten sense wire of 45 μm diameter. The tubes are filled with a 80% Argon and 20% CO_2 gas mixture, and the anode wire is tensioned at the operating voltage of 2.3 kV.

Ionizing particles crossing the tube will produce electrons (ions) which will drift to the anode wire (cathode) with a well known drift velocity (few $cm/\mu s$ for electrons), thus a radial measurement of the distance from the crossing particle to the wire is performed using the signal of the TDC board connected with each wire. The intrinsic drift time measurement error gives a spatial single tube resolution better than 300 μm (rms). The single tube hit efficiency η has been measured to be larger than 98%, while the single tube track efficiency, i.e. the product of η and the probability ϵ that the hit gives the correct drift radius, is 90%.

2.2.3 Veto

Before reaching the OPERA target, CNGS neutrinos may interact in the rock, in the mechanical structures and in the Borexino detector, producing secondary particles able to induce false triggers. In order to reject these events, a VETO system is placed upstream of the detector. The VETO is made of two planes of glass Resistive Plate Chambers (GRPC) of 9.6×9.2 m^2, each one with 32 GRPC units. Each plane is equipped with horizontal and vertical copper strips with a pitch of 2.5 cm.

2.2.4 Target

The target is based on the ECC technique, fulfilling the requirements of high granularity and micrometric resolution, necessary to distinguish the τ decay vertex from the neutrino interaction vertex. The excellent emulsion spatial ($\sim$ 1 μm) and angular ($\sim$ 2 $mrad$) resolutions are ideal for detection

of short-lived particles. The use of passive material, combined with high accuracy tracking devices, allows for momentum measurement of charged particles via multiple Coulomb scattering (MCS), for electromagnetic shower and particle identification. Thus, the brick acts as a standalone detector, that can be selectively removed from the target, developed and analyzed.

Emulsion

Nuclear emulsions consist of AgBr crystals scattered in a gelatine bender. The AgBr crystal, of 0.2 μm diameter, is a semiconductor. After the passage of a charged particle, electron-hole pairs are created in the crystal. The excited electrons are trapped in the lattice defects on the surface of the crystal and Ag metal atoms are created, which act as latent image centers. During the chemical-physical process known as development, the reducer in the developer gives electrons to the crystal through the latent image center and creates silver metal filaments using silver atoms from the crystal. This process multiplies the number of metal silver atoms by several orders of magnitude ($10^8 - 10^{10}$) and the grains of silver atoms, of about 0.6 mm diameter, become visible with an optical microscope. The overall emulsion area in OPERA is larger than 100000 m^2. The pouring of such a large amount of nuclear emulsion gel could not be made by hand, as it was traditionally done for past experiments. Therefore, an industrial production was set-up after an R&D program carried out in collaboration with the Fuji Film company.

An OPERA film has 2 emulsion layers (each 44 μm thick) on both sides of a transparent triacetylcellulose base (205 μm thick), as shown in Fig. 2.8. The total thickness is 293 $\pm$ 5 μm. The transverse size is (124.6 $\pm$ 0.3) $\times$ (99.0 $\pm$ 0.2) mm^2. The intrinsic position resolution of the gelatine with OPERA normal developer is about 50 nm, which corresponds to 0.35 $mrad$ as intrinsic angular resolution from the track positions at the two faces of the plastic base. The density of the gel is 2.7 g/cm^3 and the radiation length X_0 is 5.0 cm. The currently achieved grain density of the machine-coated

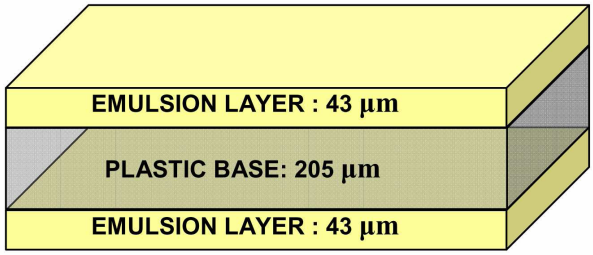

Figure 2.8: Opera nuclear emulsion: two emulsion layers coat both sides of a triacetylcellulose transparent base.

emulsion films is 30 grains/100 μm. The sensitivity of OPERA emulsion films is measured to be $\sim$ 28 grains/100 μm for minimum ionising particles.

Nuclear emulsions integrate all tracks (cosmic rays, environmental radiations) from their production to their development. During the production process at the Fuji Film industrial plant in Japan, each films integrates about 3000 tracks/cm^2 from the cosmic ray flux, a value much larger than the maximum density of about 100 tracks/cm^2 allowed for an unambiguous interaction reconstruction. In order to reduce this background, a new procedure called refreshing was set up. It consists in keeping the emulsion films at high relative humidity (RH) and high temperature. To process about ten millions films, needed for the experiment, a refresh facility was constructed in Tono mine in Gifu, Japan. The facility operates at 27°C with a cycle lasting five days: one day of open air humidification (90% RH), three days of closed air humidification (98% RH) and one day of dry mode (40% RH). This process reduces the integrated number of tracks from $\sim$ 3000 to less than 100 tracks/cm^2, without affecting the emulsion sensitivity to tracks detected later on. The randomly distributed grains (fog) induced by thermal excitation constitute a background for tracking. The fog density is slighty increased by refreshing; measurements show a fog density of 3 and 6 grains per 1000 μm^3 of emulsion, respectively before and after the refreshing.

The films treated in Tono mine were transported to Italy by boat; during

the travel, the films were placed vertically to minimize the integrated cosmic ray flux. Nevertheless, a cosmic ray density of about 1000 tracks/cm^2 was accumulated. To suppress this background, the films were vacuum packed without any spacer before the shipment. Each pack is used for one brick so that, once the films are interleaved with the lead plates, the tracks accumulated during transportation are seen with a different alignment, and therefore can be eliminated at the analysis level.

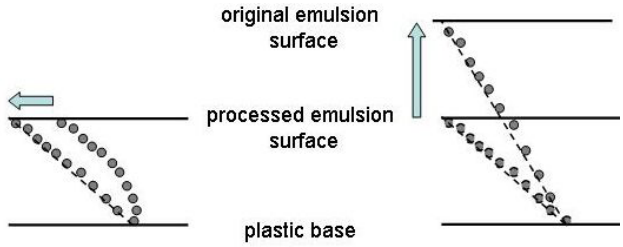

Figure 2.9: Track distortion correction (left) and shrinkage correction (right).

In order to ensure good resolution measurements, two effects have to be taken into account: *distortions* and *shrinkage* (Fig. 2.9). Distortion is a phenomenon which shifts the position of the recorded trajectories in the emulsion layer because of stresses accumulated in the gelatine layer. The simplest form of general distortion is a uniform shear: straight tracks remain rectilinear but their direction and length change by an amount which depends on the magnitude and direction of the shear. A more serious source of error is due to differential shear of the emulsion in which both the magnitude and direction of the shear change with depth. Such distortion changes the tracks of an energetic particle from a line into a curve.

The shrinkage effect is due to a reduction (or increase) of the emulsion thickness after the development process.The shrinkage factor is defined as the ratio between the values of the thickness of the emulsion before and after the development. This factor is taken into account by the tracking algorithm (the measured track slopes must be multiplied by this factor to obtain the real value).

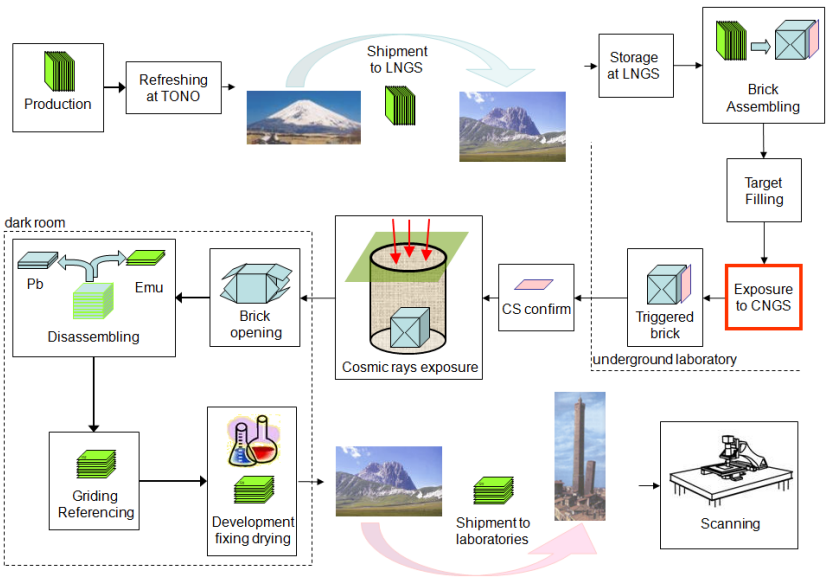

Figure 2.10: to be inserted

Emulsion Cloud Chamber

The OPERA ECC is called "brick" and is made of 57 OPERA emulsion films interleaved with 56 lead plates, each of 1 mm thickness. The transverse size of the brick is 128 $\times$ 102 mm^2, while the longitudinal size is 79 mm corresponding mass is 8.3 kg and 10 X_0 (Fig. 2.11).. The dimensions of the bricks are determined by conflicting requirements: the mass of the bricks selected and removed for analysis should represent a small fraction of the total target mass; on the other hand, the brick dimensions should be large enough to contain the primary and decay vertexes and provide particle identification and kinematical reconstruction of the event.

The brick thickness in units of radiation lengths is large enough to allow electron identification, through their electromagnetic showering, and momentum measurement by multiple coulomb scattering, following tracks in consecutive emulsion-lead cells.

The plate material is a lead alloy with a small calcium content to improve its mechanical properties; the choice of PbCa with respect to other compounds was motivated also by its low α activity, which was extensively

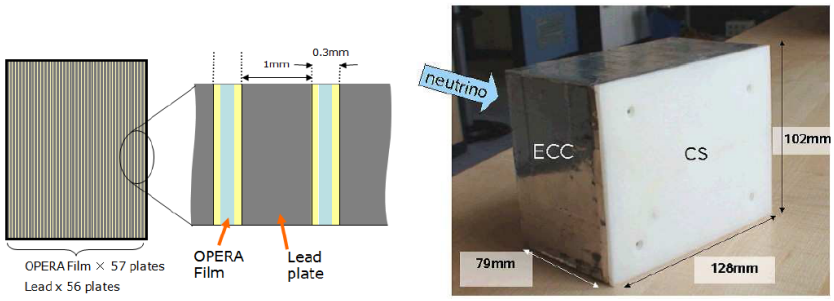

Figure 2.11: Left: schematic view of a brick in the target. Middle: blow-up insert showing two emulsion films and one lead plate. Right: photograph of a real brick as produced by the BAM.

studied [36].

A total number of 150036 bricks was assembled by a dedicated Brick Assembly Machine (BAM) composed by anthropomorphous robots, ensuring a high precision in the piling up; each of them was placed in the brick walls, ultra-light stainless-steel structures positioned between the TT planes. An automated system called Brick Manipulator System (BMS) takes care of the target walls filling and of the extraction of bricks with a candidate ν-interaction. Two BMS robots are placed on the side of the detector and can load and unload bricks on each row of the walls, by a small vehicle equipped with a suction grip.

Changeble sheet

A CS is an emulsion tracking detector attached to the downstream face of the brick and which can be removed without opening the brick, acting as interface between the electronic detectors and the brick itself. The CS concept was successfully applied to all past hybrid experiments like E531, CHORUS and DONUT. Its principal task is to confirm that the brick predicted by the electronic detector is the interaction one, thus acting as an off-line trigger for the event reconstruction. If tracks related to the neutrino interaction are observed in the CS, the brick is dismantled and developed and the tracks are

followed back until the vertex is located; if no signal is found, another CS is attached to the brick, which is reinserted into the detector. This allow to reduce the emulsion scanning load and to save the detector target mass.

CS make possible the jump from the resolution of the order of 1 cm of the TT to the 1 μm spatial resolution of nuclear emulsions. Furthermore, given the accuracy of the target tracker, the search of event tracks in the brick would be quite difficult, due to the poor signal to noise ratio resulting from the integration of alignment cosmic rays, without the help of CS.

In order to accomplish the tasks for which it was designed, the CS detector needs to have an extremely low background level; for this reason it was assembled in a dedicated facility in the LNGS underground laboratory. It consists of two emulsion films called "CS doublet" (CSd), inserted in a plastic box attached to the downstream side of the brick. The films are the same as the ones used for ECC bricks, but an additional refreshing process has been applied in the facility to further reduce the background. The refreshing conditions are the same as in the Tono refresh facility. The two films are packed in a light-tight envelope made of aluminum-laminated paper, which is then put into a plastic box attached downstream of the ECC brick. The physical background, coming from cosmic ray tracks and Compton electrons from enviromental radioactivity, is reduced to $\pm$ 100 tracks/cm^2/film. Requiring tracks aligned in the two emulsion films (4 emulsion layers) further reduces this background to about 10^{-4} tracks/cm^2, which motivated the choice of two films rather than only one.

Since CSd cannot be exposed to alignment cosmic rays as it's done for bricks, in order to save the needed high purity, the alignment between the films is achieved by printing four X-ray circular spots with a radius of 150 μm on the CS-doublet just after the brick extraction, i.e. when the CSd is still attached to the brick. The X-rays penetrate the two CS films and the most downstream film of the brick, allowing in this way also to perfom the CS-to-brick connection.

2.3 Operation mode

OPERA has a low data rate from events due to neutrino interactions well localised in time, in correlation with the CNGS beam spill. The synchronization with the spill is done offline via GPS. The detector remains sensitive during the inter-spill time and runs in a trigger-less mode: events detected out of the beam spill (essentially cosmic-ray muons) are used for monitoring and can be tagged in CS and brick emulsions. The global DAQ is built as a standard Ethernet network whose 1147 nodes are the Ethernet controller mezzanines plugged on control boards interfaced to each sub-detector specific front-end electronics. A general 10 ns clock synchronized with the local GPS is distributed to all mezzanines in order to insert a time stamp to each data block.

The event building is performed by sorting individual sub detector data by their time stamps and looking for temporal coincidences between them. A software algorithm selects events inside the target; if a muon is reconstructed by the electronic detectors the event is classified as Charged Current (CC), otherwise it is classified as Neutral Current (NC) (Fig. 2.12). The muon reconstruction efficiency by electronic detectors is about 95%.

When a trigger in the electronic detector is compatible with an interaction inside a brick, a software reconstruction program processes the electronic detector data to build a probality map of the bricks, where probably the neutrino interaction occurs. Moreover, for events with a muon in the final state (CC), a prediction for the slope of the muon and its impact on the CS is also given; for NC events, the averaged center of TT hits provides the impact point of the "hadron shower" on the CS.

The brick with the highest probability are removed from the target walls by the BMS and exposed to X-rays for CS-to-brick alignement (as explained above) and the CS doublet is detached from the brick and developed underground. The corresponding CS films are then analysed to validate the designated brick. In the meanwhile the brick is stored underground in a shielded area to reduce the integration of cosmic rays, waiting for CS scanning feed-

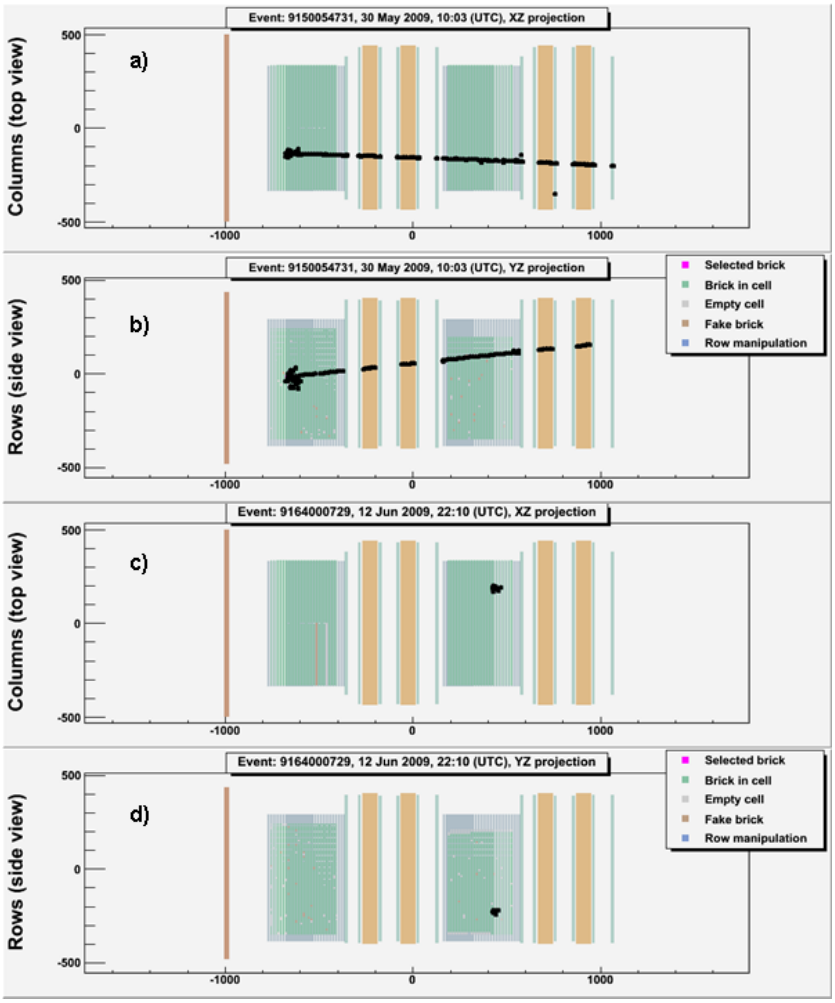

Figure 2.12: Whole detector display in x - z (a) and y - z (b) projections for an event classified as CC. (c) and (d) show x - z and y - z projections respectively, for a NC event.

back. If the CS do not confirm the interaction, the brick is equipped with two new emulsion sheets and placed back in the detector. The scanning of the CS is done in two laboratories (Scanning Stations), one at LNGS, equipped with 8 European Scanning System (described in 2.4), and the other in Japan; each scanning station analyses half of the events collected by OPERA.

After a brick has been validated, it is exposed to a lateral X-ray reference mark set (which will provide a reference system during the scanning) and then it is brought to the surface to be exposed to high-energy cosmic-rays. Cosmic rays exposure is needed in order to obtain a precise film-to-film alignment, and is performed placing the the brick, with the emulsion, perpendicular to cosmic rays, under a shielding structure (the cosmic pit) made of iron and plastic slabs used to absorb soft radiation. The exposure lasts 12 hours, corresponding to about one penetrating track per mm^2 in the angular acceptance relevant for the scanning. The brick emulsion films are then developed with an automatic system in parallel processing chains and then dispatched to the various scanning laboratories of the Collaboration.

2.4 Automatic Scanning System

In the OPERA scanning laboratories the emulsion measurements are performed by automatic scanning system. The automation of the scanning is needed by the large ammount of emulsion to be scanned in a massive detector like OPERA. Two different approches has been followed by Japanese and European groups, leading to scanning system with simlar time performances and tracking efficiencies: the so called Super-UTS in Japan and the European Scanning System (ESS) in Europe. The philosophy of ESS is, differently from Super-UTS, to use the *state-of-art* commercial hardware and software components, conceived in a modular structure, in order to achieve the flexibility needed to upgrade the system following the technological progress.

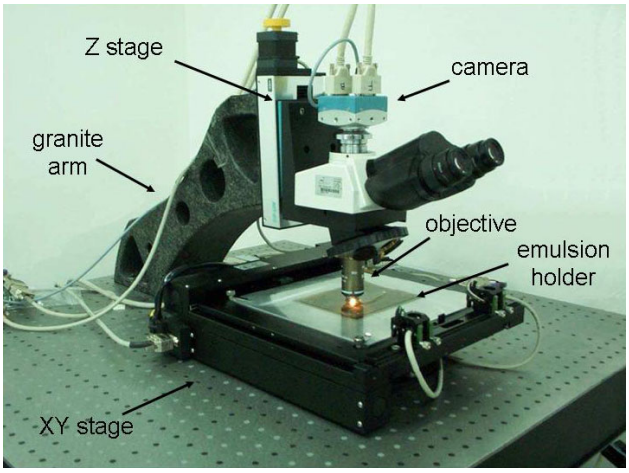

Figure 2.13: A picture of the European Scanning System

2.4.1 European Scanning System

The main components of the ESS microscope are (Fig. 2.13):

- a high quality, rigid and vibration free support table holding the components in a fixed position;
- a motor driven scanning stage for horizontal (XY) motion;
- a granite arm which acts as an optical stand;
- a motor driven stage mounted vertically (Z) on the granite arm for focusing;
- optics;
- digital camera for image grabbing mounted on the vertical stage and connected with a vision processor;
- an illumination system located below the scanning table.

The emulsion is hold by a glass plate and its flatness is guaranteed by a vacuum system. Moving continuously the focal plane of the objective through

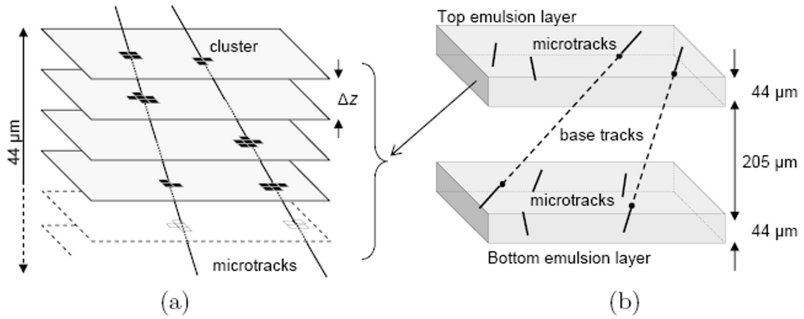

Figure 2.14: Microtrack reconstruction in one emulsion layer by combining clusters belonging to images at different levels, on the left. On the right, Microtrack connections across the plastic base to form base tracks.

the 44 μm of the emulsion thickness, a sequence of 15 tomographic images of each field of view, taken at equally spaced depth levels, is obtained.

The images acquired are then converted into a gray scale of 256 levels, sent to a vision processor board, hosted in the control workstation, and analyzed to search sequences of aligned grains (clusters of dark pixels of given shape and size). Some of this grains belongs to tracks, others, most of them, are accidentally developed single grain (*fog*, see previous section).

A *microtrack* is defined as a three-dimensional sequence of grains, on a single emulsion layer, which is reconstructed by combining clusters belonging to images at different levels and searching for geometrical alignments.

Microtracks on the top and bottom emulsion layers are then connected across the plastic base to form the *basetracks* (Fig. 2.14). Track position and slope is determined by a linear fit to these tracks.

The ESS has been designed following the specifications of:

- high speed computer controlled precision mechanics for both horizontal and vertical stages with submicron accuracy in order to move from one field of view to the next in less than 0.1 s;

- standard optical system but customized for the observation of two 44 μm emulsion layers interleaved with a 205 μm plastic base.

- high-resolution camera interfaced with a high-speed frame grabber and a vision processor able to grab and process images at rates > 350 frames per second (fps).

2.4.2 Mechanical stages

Horizontal stage.The ESS uses a Micos MS-8 scanning table with 20.5 cm range in both directions. The coordinates are read out by two linear encoders with a resolution of 0.1 μm. External optical limit switches are mounted on each axis and manually set. The motion of the horizontal stage (maximum speed, acceleration, deceleration) was set in order to minimize the time needed to move from one field of view to the next (typically ~ 350 μm).

Vertical stage. The vertical stage is the Micos LS-110 model. It is equipped with a linear encoder (resolution 0.05 μm) and limit switches. During data taking, the vertical stage moves at constant speed calculated by taking into account the camera frame rate, the number of desired frames and the emulsion thickness (44 μm). With a frame rate of about 400 frames/s and 15 levels per emulsion layer, each image is acquired at a vertical distance of about 3 μm; the resulting speed is about 1150 $\mu m/s$; the time needed to scan an emulsion layer is about 55 ms (including the time for acceleration, deceleration and synchronization with the host).

2.4.3 Optical system

The main components of the optical system are an objective, a lightning system, a condenser with aperture diaphragm, a glass window that hold the emulsion, a tube lens and a digital camera (Fig. 2.15).

Objective. The parameters that characterize an objective are: the numerical aperture (NA) that defines the ultimate image resolution (the minimal distance between two points seen as separate), the working distance (WD) and the magnification (M). The requirements for an objective that

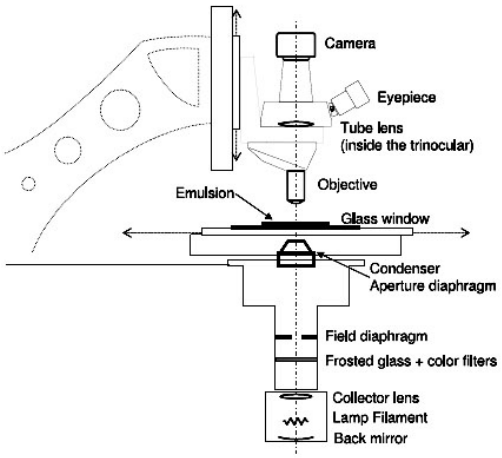

Figure 2.15: Schematic layout of the ESS microscope optical system

must read an OPERA emulsion are NA > 0.8 since a submicron resolution is needed, a WD > 0.3 mm (defined the overall thickness of emulsion layers and plastic support) and a magnification that depends on the image sensor size; for a 20 mm wide megapixel sensors an objective with M > 40 is useful to cope with the requirements of few pixels per micron and a large field of view in order not to reduce the microscope speed. During the scanning of the bottom layer of the emulsion, the whole plastic base and the top emulsion layer lay between the objective front lens and the focal plane, for a total thickness of 0.3 mm, while for the scanning of the top emulsion layer there is no intermediate medium. This variation of the thickness of intermediate medium has the effect to overcorrect or undercorrect the spherical aberration. This effect is well corrected by using an immersion oil objective, in fact oil, emulsion and plastic base have almost the same refractive index (~ 1.5) and the optical path is almost homogeneous.

The illumination system. A transmitted illumination system is placed below the scanning table. It was developed jointly with Nikon-Italy; it was designed to obtain the Köhler illumination. The light comes from a tungsten halogen lamp with a computer controlled power supply. The image of the lamp filament is focused by a lens (collector) on the aperture diaphragm

of a condenser which concentrates the light into a cone that illuminates the emulsion sheet. A second diaphragm (field diaphragm) is adjusted to prevent emulsion illumination (and also heating) outside the field of view.

The emulsion holder. The angular resolution needed for the ESS is few *mrad*; the systematic error introduced in the angular measurement by non-planarity of the glass window (which holds the emulsion) and by misalignments between the optical components and the mechanical stage, has to be kept well below 1 *mrad*. The glass window is equipped with a vacuum system to keep the emulsion steady during the scanning, and has a thickness of 4 mm. It has a thickness tolerance of less than 10 μm per 10 cm length and its deviation from parallelism is smaller than 1 *mrad*; the flatness is of a few fringes per inch ($\sim$ 0.5 μm per 1 cm). A 1 mm wide groove in the glass along the emulsion edge is connected to a vacuum pump. The stages and the optical axis are aligned with respect to the glass window (used as a reference plane).

Camera. The goal of 20 cm^2/h scanning speed requires a frame acquisition time < 4 ms and megapixel resolutions. The ESS is equipped with a Mikrotron MC1310 4 high-speed megapixel CMOS camera with Full Camera Link interface. Its image sensor is the Micron MT9M413 which delivers up to 10-bit monochrome 1280 $\times$ 1024 images at over 500 frames per second. The sensor size is 20 mm (along the diagonal) and its pixels are 12 $\times$ 12 μm^2 large. This choice follows a detailed R&D work with a custom FPGA-driven camera equipped with the same sensor.

2.4.4 On-line acquisition software

The online DAQ software for the emulsion automatic scanning and track segments reconstruction was developed using the object-oriented C++ language. It is based on a modular structure where each object carries out a well defined task. The list of all modules with their functionality is given in Tab. 2.2.

Module	Functionality
Objective	stores the information relative to the used objective and performs the pixel to micron conversion
Odyssey	drives the Odyssey board
FlexStage	is interfaced to the stage controllers and sets the movement modalities
SmartTracker	is responsible for track pattern recognition, recognizing sequences of geometrically aligned clusters.
SmartFitter	performs the track fit.
DataIO	handles data Input/Output.
SheetMap	transforms coordinates and vectors from the current stage reference frame to the emulsion local reference system defined by a grid of fiducial marks printed on the emulsions.
VertigoScan	is the steering module,which uses all the other objects to control the scanning.

Table 2.2: List of modules composing the on-line acquisition software.

The scanning output is a collection of raw data files (in binary format) which are saved in an Oracle Data Base.

Image processing

At present, a camera frame rate of 377 fps and 8-bit gray level images are used, corresponding to an acquisition rate of 471 MB/s. By acquiring 15 frames per 44 μm emulsion layer, an acquisition time of $\sim 40\ ms$ is used for each field of view. Considering a synchronization time of 15 ms, a mean time of $\sim 90\ ms$ for the field of view change, a field of view of about $390 \times 310\ \mu m^2$ and a superposition between contiguous fields of 30 μm, a scanning speed of about 22 cm^2/h is obtained. The effective scanning speed is a bit lower (~ 20 cm^2/h) because sometimes the microscope has to scan the full sheet thickness

to find the emulsion surfaces (focusing). The selected exposure time is limited by grain size ($\sim 1\ \mu m$) and by vertical resolution ($\sim 3\ \mu m$). Therefore, the exposure time should be smaller than the time needed to span 1 μm. In our working condition the exposure time is smaller than 0.5 ms (the exposure time depends on the microscope and it ranges between 0.15 and 0.5 ms). Once grabbed, each image is analyzed using image processing techniques like filters, binarization and clustering; the grains are recognized as clusters of black pixels. The number of clusters available for tracking depends on the threshold and on the selection cuts in the cluster area. Taking into account the acquisition speed and the Z level distances ($\sim 3\ \mu m$) the cluster area cut is chosen in order to maximize the grain finding efficiency (normally 3 or 4 pixels).

Tracking

The following step lies on combining different levels to recognize geometrical aligment. The tracking efficiency depend on the distortion of the tracks; the algorith should be enough flexible to take into account this possibility. The field of view is divided in cells of about 20 μm. The clusters alignment is required in the same cell or in adjacent cells. The search starts with the combination of all the clusters in two external levels and then others clusters in the intermediate level are required. The requested tollerances for the alignment depend on the emulsion charateristic and on track quality. After found this first alignment, the algorith search for further aligned clusters in other levels by means of the prediction based on the fit of the track. In principle determining if a clusters belongs or not to a track, wuold require the determination of the distance in the tridimensional space between the position of cluster and the fit of the track. Actually, because all the clusters lie in the same plane, it is possible to simplify the problem to a two dimensional one, so reducing the calculating time.

The line representing the track could be parameterized like $\mathbf{I}+z\mathbf{T}$, where $\mathbf{I}$ represent the intercept of the track with the $z = 0$ surface and $\mathbf{T} = (s_x, s_y, 1)$

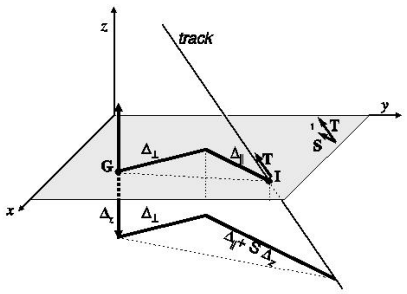

Figure 2.16: The distance between a grain **G** and the fit of the track on the z-y plane has two component: longitudinal and tranverse with respect to the track. The tranverse one does not depend on track slope.

is the slope vector. Called **S** the projection of **T** on the z plane, it is possible to introduce two versors $n_{\parallel} = (n_x, n_y)$ so that $\mathbf{S} = Sn_{\parallel}$ and $n_{\perp} = (n_y, -n_x)$, that define a naural reference system for the tracks. In this reference system the distance of a grain **G** from the track can be expressed as $\Delta_{\perp} n_{\perp} + (\Delta_{\parallel} + S\Delta z)n_{\parallel}$, where $\Delta_{\perp}$ and $\Delta_{\parallel}$ represent the tranverse and longitudunal distances in the plane of the grain (Fig. 2.16). Because the tranverse distance does not depend on the slope of the track, its average value could be used as estimator of the quality of the track. After searching clusters on all possible levels, the tracking process ends and the number of found clusters is compared with a threshold. Tracks with cluster less than 6 are rejected. The same cluster could belong to different tracks. After all the tracks in a field have been reconstructed, geometrical distortion have to be corrected. The tracks that passes throughout the whole thickness of the emulsion are used to estime the distortion vector, used to correct the position of the clusters of all the tracks in the current field. This correction is based on the assumption that the track slope in the exit point from the emulsion is the real particle slope. Another geometrical distortion is due to the development process: the shrinkage that

has to be taken into account in the reconstruction of the track slope.

2.4.5 The off-line track processing

The positions and angles of the detected tracks, for each emulsion layer, are recorded as microtracks and are connected off-line to form basetracks, whose positions and angles are not affected by distortions. After, basetracks in a series of emulsion films are collected, the films are aligned and track reconstruction (volume tracks) is performed.

Basetrack reconstruction

The automatic microscope analysis provides the microtracks in the top and bottom layers of the emulsion film. The next step is to combine microtracks in pairs in order to obtain the basetracks: microtrack pairs are projected across the plastic base. For each couple of microtracks a χ^2 is calculated as

$$\chi^2 = \frac{1}{4}\left[\frac{(\theta_{xt}-\theta_{xB})^2}{\sigma_x^2} + \frac{(\theta_{xb}-\theta_{xB})^2}{\sigma_x^2} + \frac{(\theta_{yt}-\theta_{yB})^2}{\sigma_y^2} + \frac{(\theta_{yb}-\theta_{yB})^2}{\sigma_y^2}\right] \quad (2.1)$$

where $\theta_{xt(b)}$ and $\theta_{yt(b)}$ are the projections of respectively top (t) and bottom (b) microtrack angles in the z-x and z-y planes, θ_{xB} and θ_{yB} are the same projections for the basetracks (B) and σ_x and σ_y are the microtracks angular resolutions obtained for the distribution of the angular difference between microtracks and basetracks. If for one top microtrack more than one bottom candidate microtrack is found, more than one basetrack can be reconstructed; in such a case the one with the smaller χ^2 is selected.

Emulsion film alignment

The mechanical accuracy of film piling in brick assembly is about 50-100 μm. Emulsion films are affected by environmental conditions, such as temperature and humidity, which may modify their original size; these effects

must be taken into account as they could be the source of misalignments and deformations. To this extent, by computing a set of similar transformations (shift, rotation and expansion) relating track coordinates in consecutive films, it is possible to define a global reference system prior to track reconstruction. From a set of independent measurements in single emulsion films, an aligned volume is created through an iterative pattern matching procedure computing the parameters of the transformations

$$\begin{pmatrix} x^{brick} \\ y^{brick} \end{pmatrix} = \begin{pmatrix} a_{11} & a_{12} \\ a_{21} & a_{22} \end{pmatrix} \begin{pmatrix} x^{film} \\ y^{film} \end{pmatrix} + \begin{pmatrix} b_1 \\ b_2 \end{pmatrix} \tag{2.2}$$

where x^{film}, y^{film}, are single film track coordinates and x^{brick}, y^{brick} are the corresponding aligned ones. A least square fit is applied after maximising the number of matching pairs within predefined position and slope tolerances measured in three zones, typically chosen at the corners of the scanned area in order to maximise the lever arm and thus disentangle the contributions due to rotation and traslation. Once all plates are aligned, the track reconstruction algorithm finds and fits all the measured basetracks of an emulsion film extending in both directions of the brick. In this way a number of connected basetracks (not necessarily adjacent) forms a volume-track.

2.5 Physics Performances

2.5.1 τ detection and signal efficiency

The signal of the occurrence of $\nu_\mu \to \nu_\tau$ is the charged current interaction of ν_τ in the detector target ($\nu_\tau N \to \tau^- X$). The reaction is identified by the detection of the τ lepton. The τ channels investigated by OPERA are the electron, muon and hadron channels:

Channel	Branching ratio
$\tau^- \rightarrow e^- \nu_\tau \overline{\nu}_e$	17.8%
$\tau^- \rightarrow \mu^- \nu_\tau \overline{\nu}_\mu$	17.7%
$\tau^- \rightarrow h^- \nu_\tau (n\pi^0)$	49.5%
$\tau^- \rightarrow h^- h^- h^+ \nu_\tau (n\pi^0)$	15.0%

Table 2.3: Branching ratio for τ decay.

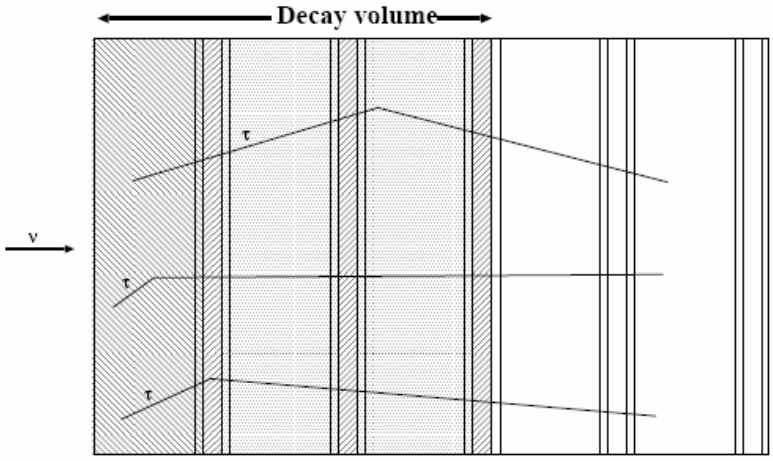

Figure 2.17: Different decay topologies; short decay (left-hatched region); long decay in base (right-hatched region) and long decay outside the base (shaded region).

The τ decays inside the ECC are classified in two categories: long and short decays. Short decays correspond to the case where the τ decays in the same lead plate where the neutrino interaction occurred. The τ candidates are selected on the basis of the impact parameter (IP) of the τ daughter track with respect to the interaction vertex, considering that the IP of primary tracks is smaller than 12 μm after excluding tracks produced by very soft particles. In long τ decays, decay occurs in the first or second downstream lead plate. τ candidates are selected on the basis of the detection of a reasonably large kink angle between the τ and the daughter tracks (θ_{kink} ¿

20 $mrad$). The analysis of the $\tau \to e$ channel benefits from the dense brick structure given by the cell design, which allows the electron identification through its showering in the downstream cells.

For the muonic decay mode the presence of the penetrating (often isolated) muon track crossing the whole detector structure allows an easier vertex finding. The potential background from large angle scattering of muons produced in ν_μ CC interactions can be reduced to a tolerable level by applying cuts on the kink angle and on the muon transverse momentum at the decay vertex.

Hadronic decay modes have the largest branching ratio but are affected by background due to hadronic interactions. One of the primary hadrons, in fact, can interact in the first lead plates and it may simulate the decay of the τ. Strong kinematical cuts are used to reduce this background.

The overall τ detection efficiency, estimated by evaluating the efficiencies related to the various steps of data reconstruction (i.e. trigger and brick finding, vertex finding, decay detection and kinematical analysis) is reported in Table 2.4.

Channel	Efficiency
$\tau \to e$	3.1%
$\tau \to \mu$	3.7%
$\tau \to h$	3.2%
$\tau \to 3h$	1.1%
Total	11.1%

Table 2.4: τ detection efficiencies for the OPERA experiment.

2.5.2 Background

Background sources to the τ detection are:

- Prompt ν_τ production in the primary proton target and in the beam dump. Prompt ν_τ originate from the decay of τ produced in the CNGS

target by the decay of D_S mesons. The rate of ν_τ production from the interaction of 400 GeV/c protons in a Be target and in the downstream beam dump has been evaluated in for the CERN Wide Band Beam. These results have been scaled down according to the features of the CNGS beam and the distance of the experiment from the source. Following the method of ...., $\mathcal{O}(10^{-6}) \times N_{CC}$ ν_τ interactions are expected, where N_{CC} is the total number of μ CC interactions. If one also takes into account the detection efficiency and the fact that the experiment will integrate $\mathcal{O}(10^4)$ events, the contribution to the background is completely negligible.

- Decay of charmed particles. Charmed particles are produced in CC and NC neutrino interactions through the reactions:

$$\nu_\mu N \quad \rightarrow c\mu X \tag{2.3}$$

$$\nu_\mu N \quad \rightarrow c\bar{c}\mu X \tag{2.4}$$

$$\nu_\mu N \quad \rightarrow c\bar{c}\nu_\mu X \tag{2.5}$$

  Charmed mesons have masses and lifetimes similar to those of τ lepton. The above processes may thus constitute a background to the oscillation signal if one fails to detect the primary muon in the reaction 2.3, the charm partner in the reaction 2.5 or both (charm and muon) in 2.4. The most relevant source is given by single charm production, i.e. the first reaction. The identification of charm particles is also a benchmark for the τ detection, since the finding efficiency is similar for both types of particles. In the subsample of events classified as CC interactions, for which the decay search analysis was performed till now, a total of 20 charm decays has been observed that survived the selection cut-offs, in agreeement with the number expected from a MC simulation, 16.0 $\pm$ 2.9. This demonstrates that the efficiency of the search for short-lived decay topologies is understood.

- Background from π^0 and prompt electrons. In addition to charm production, other sources must be considered as possible background for

$\tau \rightarrow e$ long decay: kink-like events from scattering of primary electrons produced in ν_e CC interactions and pion charge exchange process ($\pi^- p \rightarrow \pi^0 n$) in ν_μ NC interactions.

- Large angle muon scattering. Muons produced in ν_μ CC events and undergoing a scattering in the lead plate following the vertex plate could mimic a muonic τ decay.

- Hadronic reinteractions. An important source of background to the hadronic decay channel is due to reinteractions in the lead of hadrons produced in ν_μ NC interactions and in ν_μ CC interactions in which the primary muon is not identified and no visible activity at the interaction vertex can be seen. Hadron reinteractions can also contribute to the $\tau \rightarrow \mu$ channel when a hadron, produced either in ν_μ NC or ν_μ CC interactions with the muon not identified, is misidentified as a muon.

Channel	Signal	Background
$\tau \rightarrow e$	3.5%	0.17%
$\tau \rightarrow \mu$	2.9%	0.17%
$\tau \rightarrow h$	3.1%	0.24%
$\tau \rightarrow 3h$	0.9%	0.17%
Total	10.4%	0.75

Table 2.5: Expected number of τ and background events collected by OPERA in five years' data taking. Signal events are computed for full mixing and for $\Delta m^2 = 2.5 \times 10^{-3}\ eV^2$.

The contribution of the above sources to the total background depends on the actual decay channel. The total background from the listed sources, assuming the nominal beam intensity ($4.5 \times 10^{19} p.o.t.$), is estimated to be less then ~ 0.8 events in 5 years of OPERA operations.

Chapter 3

Emulsion analysis chain

3.1 Vertex Location and Reconstruction

The procedure applied in the analysis of the OPERA bricks can be sketched in the following steps:

- Changeable Sheet (CS) scanning
- CS-to-brick connection
- Scan-back
- Volume Scan and vertex reconstruction
- Vertex Definition and Decay Search

3.1.1 Changeble sheet analysis

As explained in 2.3, when a neutrino interaction occurs in the OPERA detector and is triggered by electronic detectors, a software classifies it as CC or NC, depending on whether a muon track is reconstructed or not by electronic detectors. Moreover a probability map is evaluated using electronic detector data to find the position of the brick in which the neutrino interaction took place. The brick with the highest probability is extracted from

the target, its CS doublet are detached and the brick is sent to the storage area in hall B. The CS doublet is developed and the scanned area is chosen depending on the type of neutrino interaction (CC or NC). In case of CC events an area of $6 \times 4\ cm^2$ around the predictions provided by the electronic detector is scanned. In case of NC the area is $8 \times 6\ cm^2$. The scanned are is not squared because during the exposure the vertical alignment of the bricks in the detector is guaranteed by the rail where they lay while the horizontal alignemnt is less reliable. The following step is then to reconstuct all the basetracks present in the selected area of both changeble sheets (sec. 2.4.4 and 2.4.5.

After basetrack reconstruction a first alignment between the two CS films is performed using the X-ray spots printed, soon after the brick extraction (sec. 2.2.4) and tracks crossing both CS films are searched for A coincidence of basetracks in the two different films is called *double basetrack*. To reduce the background due to random coincidences, a visual inspection of those tracks is performed with optical microscope (*manual check*) by experienced and trained operators. In order to reduce the load of manual check a statistical tool based on a likelihood method has been studied. Moreover, to recover intrinsic inefficiencies affecting the microtracks reconstruction, coincidences of a microtrack and a basetrack (*3 out 4 tracks*) belonging to different films are also taken into account. This can be done only if a micrometric alignment of the films, not available with the X-rays spots, is achieved. This micrometric alignment is obtained exploiting the low energy electrons originating from radioactive isotopes present in the emulsion, as shown in fig. 3.1.

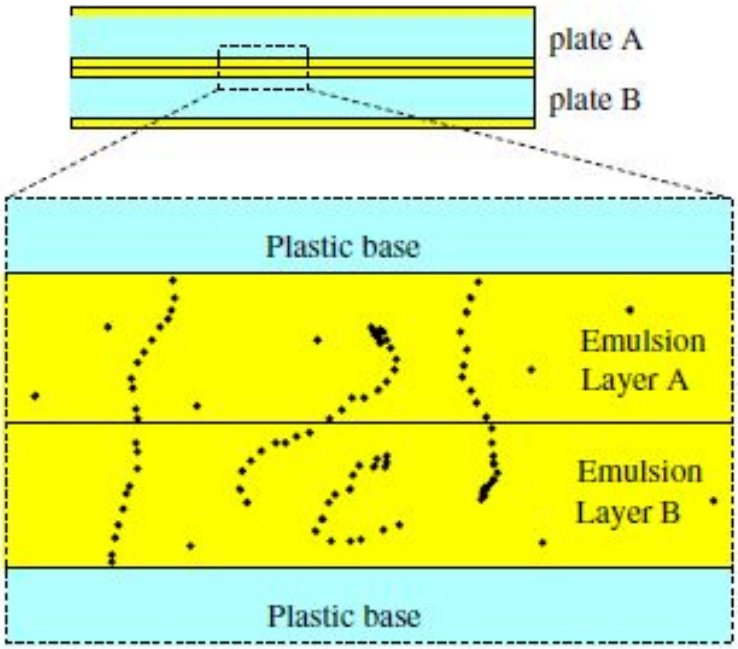

Figure 3.1: Schematic diagram of the alignment between CS films using low energy electrons.

3 out 4 tracks are also visually inspected to confirm that are formed by double basetracks wrongly reconstructed due to reconstruction algorithm or to acquisition inefficiency.

Once a track crossing both CS films is found (double basetrack or 3 out 4), the match with tracks reconstructed by electronic detector is searched for according a χ^2 method based on the slope and position residual between electronic predition and emulsion double basetracks. The basetracks belonging to muon originating from the neutrino interactions in the rock in front of detector (rock muon) or from secondary cosmic rays are rejected and the basetracks belonging to muon of the CC event are tagged (muon candidate). Finally for the event validation, one of these three conditions has to be satisfated:

- a pattern of at least two converging tracks is found;

- a muon candidate is found;
- a track compatible with an isolated 3-dimensional track reconstructed by the electronic detector is found.

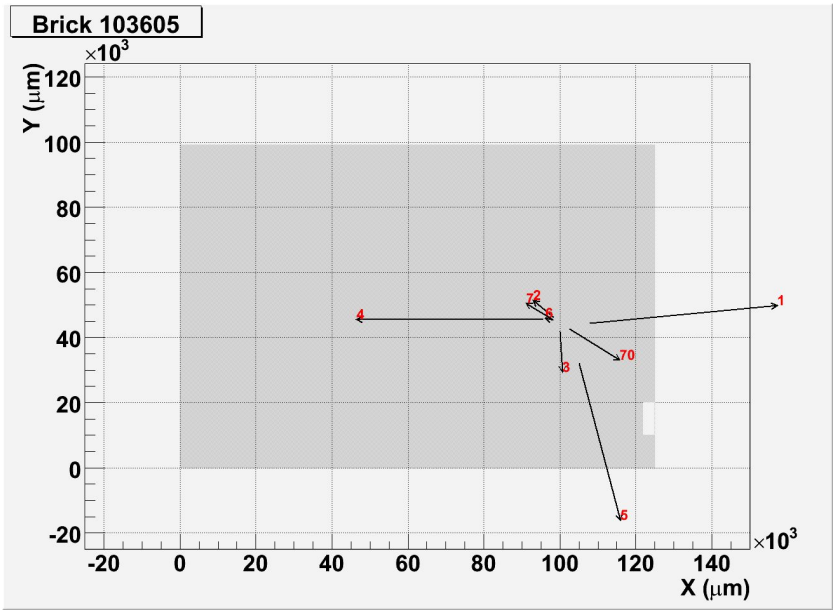

Figure 3.2: CS-display of tracks found in the CSd scanning: the grey zone is the whole surface of a CSd, each arrow represent a track, the starting point of the arrow is the position of the track, the slopes of the arrow are proportional to the slopes of the track. The track with id 70 is a muon candidate. In this case, also a clear pattern of converging tracks has been found.

If no signal is found, the brick is sent back to the detector with a new CS attached and the analysis proceeds with an additional brick request. In case one of the three previuos conditions are fullfilled, the analysis follows as explained in 2.3, i.e. the brick is unpacked and its films are developed and sent to the scanning laboratories the information about electronic reconstruction and CS scanning are stored in a central database accessible by all laboratories.

3.1.2 CS to brick connection

Once the brick emulsion and the relative CS information are available, the *CS-to-brick connection* procedure is performed in the scanning laboratories. This procedure is conceived to link the signal basetracks found in the CS doublet with signal basetracks in the emulsions of the bricks, among the physics background basetracks due to cosmic rays. It represents a very crucial phase due to the fact that CS are 4500 μm far from the brick put inside a plastic box roughly aligned to the brick. The CS double basetracks are projected to the z plane of the four most downstream (with respect to the neutrino beam direction) emulsion in order to obtain predictions to be searched for. A small area of $2 \times 2\ mm^2$ is scanned around each predictions and each films. All the basetracks within 300 μm a the prediction and with a slope within 30 $mrad$ are visual inspected to discard fake basetracks. The tolerances correspond to 3σ of the position and angular residual distribution obtained using $\sim$ test bricks during the commissioning of the experiment. If a basetrack is confirmed then is projected to most downstream film to check on one hand if they are compatible with the CS predictions in the most downstream film within the previous tolerances and on the other hand if basetracks from different film belong to the same track candidate or not. All track candidates are selected to be the input of the scanback procedure.

3.1.3 Scanback procedure

The procedure to localize the neutrino interaction point inside the brick is called *scanback procedure*. CS candidates connected to bricks are followed up, plate-by-plate until their disappearance. This condition is a clear signal that "something" happened at this point.

Scanback starts from track position and slopes in the most downstream sheet and then the track coordinates in the next upstream plates are predicted.

An automatic scanning system searches for basetracks compatible with

the predicted tracks by scanning a single microscope view centered at the expected position. The torelances for the selection of the candidate basetrack is $\Delta x(\Delta y) = (80 + 6 * \theta_x(\theta_y)(\mu m)$ and $\Delta\theta_{x,y} = (30 + 50\theta_{x,y})(mrad)$.

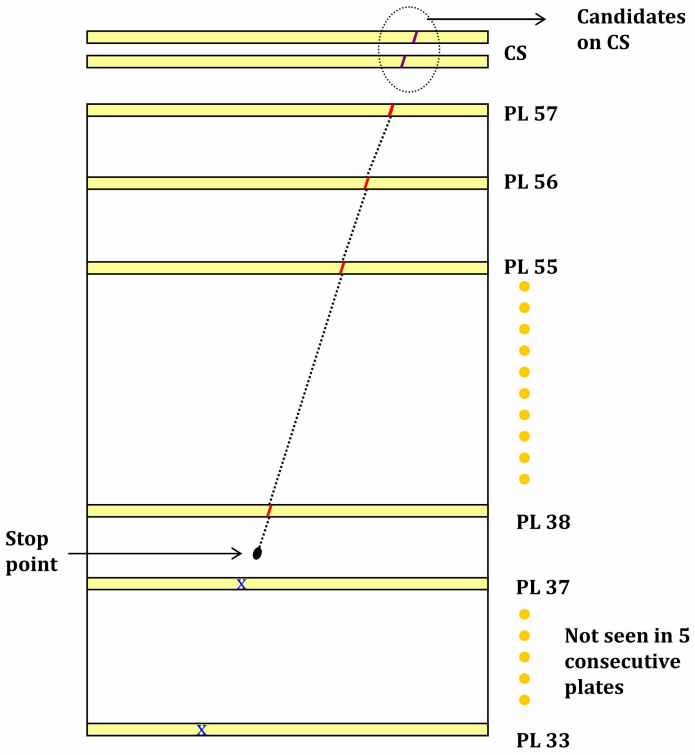

Figure 3.3: Schematic representation of the Scan-back procedure. The track segments (in purple on CS doublet and in red on the brick) are seen just on the emulsion sheet (yellow) and not in the lead plate (white). When the track disappear for 5 consecutive plates the interaction point is located

The newly found basetrack is projected on the next emulsion film surface in order to obtain a prediction for the basetrack to search. The process is iterated until one of the following conditions occurs:

- No segments are found in at least five consecutive plates. The last plate

where the track is reconstructed is called *scanback stopping point*. The request to scan at least 5 plates upstream the scanback stopping point is due to redusce the fake scanback stopping point due to reconstruction algorithm or acquisition inefficiencies. Consiering an acquisition efficiency of $\sim 80\%$, the number of "fake stop" after checking 5 plates is $\sim 0.4\%$. Futhermore manual checks are performed on the scanback stopping point in order to check the goodness of the track reconstruction (sometime it may happens that the basetrack is reconstructed with wrong parameter (i.e. slope) or a background basetrack is selected). Also the plates upstream with respect to the stopping point are manually checked to confirm the stopping point.

- The track exits the brick. It means that the neutrino interaction did not take place in the brick under examination, but in another one, namely the upstream one or an adjacent brick, respectively if the track exits from the most upstream plate ("passing-through") or through an edge ("edge-out"). Another brick is extracted, and its CS doublet is also scanned, searching for more tracks related to the event; the vertex location procedure is repeated as explained for the first brick. A fraction of the neutrino interactions occurs in the target frame, or in the target tracker detector; such events cannot be used for neutrino oscillation search, because the vertex region cannot undergo topological analysis.

It is to be noticed that these procedures (scanback and CS-to-brick connection) is based on two assumption:

- the position and slope of the upstream basetrack can be predicted by the downstream one.
- the energy of the track is enough to reach the downstream emulsions of the emulsion and the changeble sheets

These condition are well satisfied by high energy penetrating particle, such as muons or hadrons, for which the procedure has been thought. On the

other hand primary electrons are subject to the bremsstrahlung process, so their plate by plate scattering could be over scanback tolerances, moreover the brick length is equivalent to 10 radiation lenght so for very upstream event the electromagnetic shower originating from primary electrons could be totally included in the brick. This aspects make scanback procedure less efficient (for neutrino interaction point localization) in events where only electrons basetrack are available (such as ν_τ CC interation where the τ decay into electron or ν_e and $\overline{\nu}_e$ CC interation)

3.1.4 Volume scan and vertex recontruction

Once a scanback stopping point has been found, the *totalscan* procedure is applied in order to confirm or disprove the interaction and study the topology. A volume scan is performed over a $1 \times 1\ cm^2$ area in 5 films upstream and 10 downstream of the stopping point.

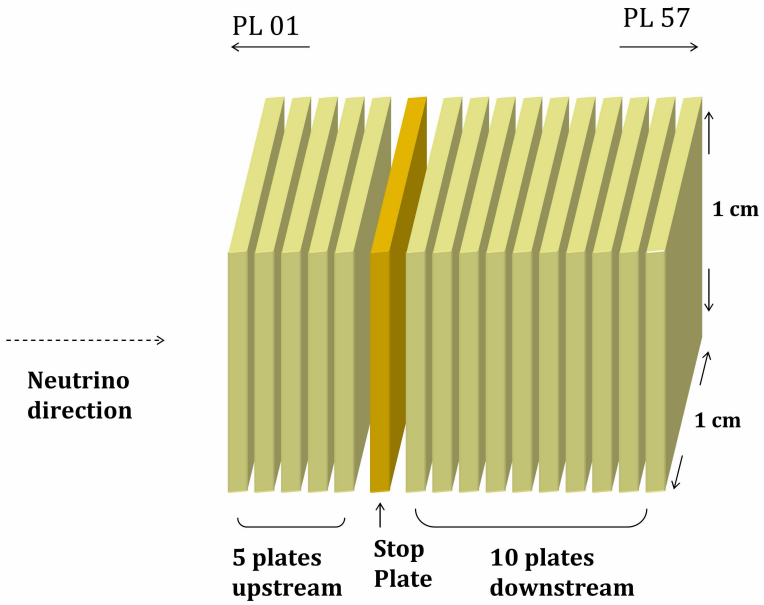

Figure 3.4: Schematic representation of a total scan volume. 1 cm2 is scanned around the stopping point on 10 plates downstream and 5 upstream with respect to the lead plate in which the interaction supposed to be

Track segments (basetracks and microtracks) are measured within an angular acceptance of 0.6 *rad*. Basetracks are reconstructed in each emulsion films then the films are aligned, with micrometric precision using high penetrating cosmic ray tracks at which the brick is exposed just before the development; tracking and vertexing are finally performed. Reconstruction of tracks and vertices is accomplished by an automatic software. It is to be notice that the tracking algorithm assumes straight line track propagation so it has low reconstrution efficiencies for large scattering tracks such as that due to low momentum particles or electrons. Furthermore only tracks composed by at least two basetracks are reconstructed. These features make very difficult the identification of the electromagnetic shower. The software produces an unbiased reconstruction, and every geometrical crossing of tracks is considered a possible vertex; The scanback tracks are searched among all the reconstructed tracks. Three cases can be found:

- the reconstructed scanback track belongs to a vertex with an upstream track (*parent track*). In this case the vertex is assumed to be an hadronic interaction and the scanback procedure continue with the parent track.

- the reconstructed scanback track belongs to a vertex without a parent track. In this case the vertex is the neutrino interaction vertex candidate.

- the reconstructed scanback track doesn't belongs to any vertex. In this case the neutrino interaction point is assumed to be in the upstream lead plate.

In the last two case further checks and analysis are performed to confirm the candidate vertex is the neutrino interaction vertex and if it is the case to study the topologies and to search for decay vertex.

3.2 Primary Vertex Study

3.2.1 Primary Vertex Definition

Depending on whether a multi-prong vertex has been reconstructed or an isolated muon or hadron has been found in the volume-scan data, a different procedure is applied.

Events with a reconstructed vertex

If a reconstructed vertex is found following the procedure descibed in 3.1, a procedure is applied in order to better define the neutrino interaction point. The use of the track information in the film immediately downstream of the neutrino interaction point (hereafter referred to as vertex film) is a crucial step in order to improve the resolution in the determination of its position. Track segments in the vertex film could be missing in the reconstruction because of tracking inefficiency. Moreover, electron-positron pairs coming from the conversion of γ produced in π^0 decays and pointing to the vertex can spoil its accuracy. By visually inspecting the vertex film, the parameters of the track segments recognised by eye can be measured by connecting the points closest to the plastic base and can be used to re-compute the vertex position. Furthermore, e^+e^- pairs can be identified as couples of very-close converging segments and can be thus tagged and removed in the determination of the vertex position. Once the e^+e^- pairs are discarded, the vertex point is defined as the average position of all tracks connection points.

If a track is found to have an impact parameter larger than 10 μm for a vertex depth in lead (VD) $\leq$ 500 μm or larger than (5 + 0.01 $\times$ VD) μm for VD $\geq$ 500 μm, it has to be further studied in order to investigate whether the reason for such an anomaly can be the scattering of the particle in the traversed lead thickness: an estimation of its momentum is thus performed. If enough measurements (e.g. scanback data) are available for the track, a multiple Coulomb scattering (MCS) algorithm is applied and a cut p $<$ $1GeV/c$ defines low momentum particles to be disconnected from the vertex

for a more accurate determination of its position, if the multiplicity is larger than 2. If the multiplicity equals 2, the track is not disconnected and the vertex position is determined using both particles atttached to it. If the MCS algorithm cannot be used, a check of the track angles has to be performed. By using at least 8 measured segments (further measurements are foreseen if data are not available), the RMS of the angular differences between consecutive segments is computed in the transverse (T) and longitudinal (L) planes according to the following formula:

$$\Delta\theta_{T,L}^{RMS} = \sqrt{\frac{\sum_{i=1}^{N} (\Delta\theta_{T,L})_i^2 / N_{pl,i}}{N}} \tag{3.1}$$

where $(\Delta\theta_{T,L})_i$ are the $i-th$ angular differences in the transverse and longitudinal plane, respectively; $N_{pl,i}$ is the number of lead plates between the two segments; N is the total number of angular differences. If both components have $\Delta\theta^{RMS}$ larger than 0.015 rad, the track is classified as due to a *low momentum* particle and discarded from the vertex. Otherwise, the track is followed downstream film by film until a reliable estimation of the momentum by the MCS method is obtained. If it found to be less than 1 GeV/c, the track is flagged as low momentum and discarded from the vertex.

Events with an isolated muon or hadron

If the scan-back track is not associated to any reconstructed vertex, extratracks satisfying the following criteria are selected:

- the most upstream segment is in any of the three emulsion films upstream of the scan-back track stopping point or in any of the three films downstream of it;
- the impact parameter, computed with respect to the extrapolation of the scan-back track to the centre of the upstream lead plate, is smaller than 500 μm;
- the track has at least three segments in the reconstruction.

In the case a vertex formed by one or more extra-tracks is found, the procedure described in 3.2.1 applies.

3.2.2 Decay Search procedure

Events with a reconstructed vertex

Once vertex point has been carefully defined, any track with an anomalous impact parameter that cannot be explained in terms of scattering has to be carefully investigated to check for the presence of a possible short decay, occurring in the same lead plate as the neutrino interaction.

The decay of a short-lived particle can be also detected by searching for possible daughter tracks, hereafter called extra-tracks, among those reconstructed in the measured volume and stopping therein. The selection of the extra-tracks is done according to the following criteria:

- the longitudinal distance between the vertex and the most upstream segment of the track (Δz) is smaller than 3.6 mm;
- the impact parameter with respect to the vertex is smaller than 300 μm if $(\Delta z) \leq 1$ mm, or smaller than 500 μm otherwise;
- the track has at least three segments in the reconstruction.

Additional criteria apply for NC-like events, where an ambiguity exists on the primary vertex definition. A multi-prong vertex with multiplicity 3, for example, could be the secondary vertex generated by a $\tau \rightarrow 3h$ decay, unlike for events with a reconstructed μ^-, where the neutrino interaction point is clearly identified through the muon track. If the multiplicity is lower than 3, extra-tracks satisfying the following criteria are selected as well:

- the most upstream segment is in any of the two emulsion films upstream of the vertex;
- the impact parameter with respect to the reconstructed vertex is smaller than 500 μm;

- the track has at least three segments in the reconstruction.

Extra-tracks are then inspected to filter out e^+e^- pairs from γ conversion, particles not originating in the measured volume (typically, low momentum particles reconstructed as shorter tracks due to multiple Coulomb scattering) and fake tracks due to the failure of the reconstruction program (especially for bricks characterised by a high density of random grains produced in the emulsion film development process and not belonging to particle tracks). Surviving extra-tracks originating in the vertex film are analysed to check if it is low momentum as described in 3.2.1.

A dedicated parent *search procedure* is applied to the extra-tracks starting downstream of the vertex film to detect long decays. It consists in searching for a track connecting the selected extra-track to the reconstructed vertex with an impact parameter with respect to the vertex smaller than 10 μm and a minimum distance from the daughter track smaller than 20 μm. Any candidate parent track selected according to these criteria is validated by visual inspection. The same procedure applies to extra-tracks originating upstream of the vertex for NC-like events. A search for converging tracks is also performed. The presence of possible heavy ionizing particles produced at the secondary vertex deserves a careful check for the discrimination between hadronic interactions and particle decays.

A search for possible small kinks along the tracks attached to the neutrino interaction, not automatically detected in the reconstruction of total-scan data, is performed in a fiducial volume of 4 films downstream with respect to the vertex, interesting for short-lived particles. The procedure is applied to all tracks for NC-like events. As for interactions with a reconstructed μ^- in the electronic detectors, the method is applied only to the track attached to the vertex matching the muon prediction. Track by track, the largest angular difference, $\Delta\theta_{T,L}^{MAX}$, in either projection is computed in the 4 most upstream films. Similarly to 3.1, the $(\Delta\theta_{T,L}^{RMS})_{kink}$ is then evaluated excluding such difference. If the ratio $R_{T,L} = \Delta\theta_{T,L}^{MAX}/(\Delta\theta_{T,L}^{RMS})_{kink}$ is larger than 5 in either projection and the kink angle, confirmed by direct check in emulsion,

is larger than 0.015 rad, the momentum of the particle is measured according to the same prescriptions reported in 3.2.1.

Events with an isolated muon or hadron

In case the procedure described in 3.2.1 selects an isolated extra-track, a parent particle connecting the two tracks with a minimum distance smaller than 20 ìm is searched for. If no extra-tracks are found, a search for a single parent segment with a minimum distance with respect to the scan-back track smaller than 20 μm is performed in order to recover events such as quasi-elastic ν_τ interactions with the tau particle decaying in one prong.

Chapter 4

Strategy for electron search

As explained in chapter 3, the vertex location and reconstruction is not optimaized for the location, identification and reconstrunction of electromagnetic showers. For this purpose I have contributed within a working group to define a dedicated procedure and to develop the needed tools. It consist in selecting events by searching for hints of showers during the standard process of vertex location. The location procedure is modified for selected events and an e.m. shower reconstruction algorithm is applied.

4.1 Shower trigger on changeble sheets

A first hint is defined at CS scanning level (*CS shower hint*). When an electromagnetic shower originating inside the brick reaches the CS, the basetracks of electrons and positrons show up as a bunch of tracks with similar slope and very close one another. Therefore, among the tracks reconstructed in the CS doublet, a cluster of CS double-basetracks is searched for. For each CS track, the distance and the slope difference between all the other CS tracks is evaluated. If the distance is less than 2 mm and the slope difference is less than 150 $mrad$, the track is added to the cluster: there is a CS shower hint when a cluster is formed by at least 3 tracks.

4.2 Shower trigger on scanback

The second shower hint is defined at scanback level (*SB shower hint*). There are two kind of SB shower hints:

- The first one is based on the fact that in the upstream part of the shower, where the electrons are energetic, the basetracks left in the emulsion are very near and similar even within the scanback tolerances for the selection of the upstream segments candidate. So it may happens that, during the scanback process, the selected basetrack do not belong to the same electron but it jumps from one candidate to a near one. Moreover approcching the primary of the shower all the scanback tracks belonging to the shower followed from the CS will merge into the same track, the primary electron. So among all the basetracks selected in scanback, a basetrack in common with different scanback tracks is searched for. If three different scanback tracks share the same basetrack, there is the SB shower hint
- The second kind of SB shower hint concerns the less energetic part of the shower where the electron pair could be resolved by eye. If during the check of the scanback stopping plate an electron pair is recongnized by eye there is a SB shower hint;

4.3 Electron events recovery

Another shower hint is defined using both reconstructed data and CS scanning results, and is dedicated to the identification of CC ν_e event. This kind of events present an electron originating from the primary vertex and if the electromagnetic shower initiated by the electron crosses the CS, it would show up as a cluster of tracks. The cluster will be related to the primary electron track. This feature is exploited to identify ν_e events among all NC located interactions, projecting all the primary tracks to the CS and evaluating distance and slope difference between the projection of the primary

track and all the CS candidates. If a CS tracks have a distance with respect of the projection of the primary track less than 2 mm and a slope difference less than 150 $mrad$, it will included in the cluster. There is a *VertexToCS shower hint* if a cluster is composed at least by 3 tracks.

4.4 Shower reconstruction algorithm

Once a shower hint is found, we use a shower reconstruction algorithm in order to reconstruct the electromagnetic shower. The algorithm is an iterative procedure starting from a basetrack as *seed*. The projection of the seed in the following film is then evaluated and are used as predictions on that film. All the basetrack with:

$$\Delta r < 90\ \mu m \quad where \quad \Delta r = \sqrt{\Delta x^2 + \Delta y^2} \tag{4.1}$$

$$\Delta\theta < 150\ mrad \quad where \quad \Delta\theta = \sqrt{\Delta\theta_x^2 + \Delta\theta_y^2} \tag{4.2}$$

$$\tag{4.3}$$

are selected. A quality estimator is then defined as:

$$\chi^2 = \frac{1}{2}\left(\frac{\Delta\theta_x^2}{\sigma^2} + \frac{\Delta\theta_y^2}{\sigma^2}\right) \tag{4.4}$$

where $\sigma^2 = 0.014\ rad$ has been obtained from MC simulations. All the basetracks with a χ^2 larger than 15 are discarded, the other are candidates basetracks belonging to the shower. The described procedure is then repeated with the selected basetracks as seed. This process is iterated until the algorithm do not selected any basetracks or it reaches the end of the volume.

Once the shower is reconstructed, the algorithm performs an energy estimation. In order to charaterize the shower and evaluate its energy five variable are defined for this purpose:

- the number of basetracks belonging to the shower.

- the longitudinal profile, i.e. the number of basetracks as a function of the "plate number" from the shower primary.

- the position of the devolepment of the shower, i.e. the longitudinal distance between the plate with the maximum number of shower basetracks and the plate of the shower primary.

- the tranverse profile, i.e. the basetracks density as a function of the radial distance from primary in the transverse plane.

- the slope of the lateral profile.

These variable are the input for a Neural Network (NN) developed in the ROOT framework and devoted to perfom the energy estimation. The NN is structured in 3 layers:

- the first layer is composed of 5 neurons. Each neuron is linked to an input variable.

- the second layer (the hidden layer) is made of 5 neurons too. Each of these neurons are connected to the other one of the former layer (in total 5×5 connections).

- the last layer, the output layer which provide the value of the energy. The output neuron is connected to the five one of the hidden layer.

This algorithm provides an energy estimation of the shower. The resolution (for shower devolopping in 57 films and without background) was evaluated to be:

$$\frac{\Delta E}{E} = \frac{0.246}{\sqrt{E(\mathrm{GeV})}} \tag{4.5}$$

and improving with the number of plates used in the reconstruction.

4.5 Extended volume procedure

We discussed how the presence of the shower hints would affect the location procedure when these two situation occurs:

- No CS tracks has been connected in the brick.

- No SB tracks has been reconstructed in the scanned volume.

In these two cases, the presence of any shower hint is checked. If a shower hint is found at level of SB in the second case or at level of CS for both the situation, then a more extended volume is scanned. The volume is 1×1 cm^2 for 20 plates upstream the SB basetrack with shower hint (the 20 downstream plates in case the CS to brick connection fails). The volume is reconstructed as explained in 3.1.4. The shower reconstruction algorithm is then applied to check whether there is a reconstructed shower related to a shower hint or not. If the shower is found and it is not fully contained in the scanned volume, the upstream plates are scanned until the whole shower is fully contained. If the primary track of the shower is attached to a multiprong vertex then the event is located, otherwise the primary track has to be check by visual inspection, on different plates in order to identify if the shower is due to a gamma ray or an electron. If the primary track is recognized to a be e^+e^- pair (two distinct very similar basetracks are found in manual check) then the event is rejected as a ν_e interaction. On the other hand if the primary track is recognized to be a single basetrack, the event is then localized.

Once the event is localized, in order to be able to perform a kinematical analysis, the shower energy is evaluated by the shower algorithm, as explained in 4.4. In order to get the best energy estimation a scan of all the available plates are performed, up to plate 57.

4.6 Simulation

4.6.1 OpRelease

OpRelease is the software framework of the OPERA experiment. It is written in C++ code and based on ROOT classes. It is managed by the Concurrent Versions System (CVS) and stored on the OPERA CVS repository at CERN. The OpRelease software has been built into the CMT environment, the Configuration Management Tool, that handles system configuration, dependencies and compilation. It has been conceived as a tool for both data and MC analysis and it is structurated in several sub-packages which take care of different steps in the simulation chain.

- OpNegn is the neutrino event generator in the OPERA experiment. It is based on the NEGN neutrino generator that profits from the experience of the NOMAD experiment, from which it is derived, where a large sample of ν interactions with thier final states was accumulated. The adaptations needed for the OPERA experiment include the description of the beamline, the neutrino energy and the CNGS target. The deep inelastic ν-interactions are based on a modified version of the LEPTO 6.1 generator, while the fragmentation process is described with a modified version of JETSET 7.4. Non scaling processes, like quasi-elastic and resonant interactions are described by two other sub-generators, respectively based on the Lewellyn-Smith and the Rein-Sehgal models. Nuclear re-interactions from hadrons produced in the fragmentation process are described with the Formation Zone Intra-nuclear Cascade (FZIC) code (extracted from the DP-MJET II.4 generator) and reinserted in the JETSET simulation. It is possible to choose the type of interacting neutrino and the vertex position (interaction on lead, on emulsion, on electronic detectors, on the rock, etc...). It produces an ASCII file with the kinematical information of the particles created in the neutrino interaction and those of the secondary vertices.

- OpRData describes the data format.
- OpGeom describes the geometry of the detector (size, positions and material features). A description of Borexino, the upstream experiment of OPERA with the respect of the beam direction in the Hall C of the LNGS is also taken into account.
- OpSim reproduces the particle propagation inside it with the concurrent creation of track hits in the various sub-detectors. OpSim is based on the ROOT Virtual Monte Carlo (VMC): a generalized Monte Carlo allows the user to choose the transport generator between GEANT 3.21 and Geant4, for the whole detector, or FLUKA, only for the bricks. In order to optimize the calculation time, cuts on energy discard low energy particles. For photons and electrons these cuts are looser to get a realistic simulation. The output is a ROOT file containing the "hits", i.e. the informations about any passage of a particle in the detector materials.
- OpDigit simulates the detector response. It takes into account the attenuation of the signal amplitude due to the propagation on the cables and optical fibers and converts the energy deposit on RPC gas and on emulsion respectively in the detected electric signal on the end of the "strip" and on the recorded segment in the emulsion.
- OpRec performs many tasks, such as: cross-talk removal, tagging of events on time with the beam, reconstruction of the tracks with electronic detectors, muon identification and event energy evaluation.
- OpCarac classifies the events into several classes: events with a muon coming from outside the detector, events originated in the iron of the spectrometer, border events or contained events.
- OpBrickFinding is the package predicting the brick containing the neutrino interaction. It produces a probablity map and evaluate for each brick the probability to contain the event.

- OpEmuIO simulates the scanning system and produces the microtracks. It applies the scanning system efficiencies and applies a gaussian smearing on position and slope of the microtracks in order to reproduce the measurement errors.
- OpEmuRec is the package for the emulsion data analysis.

4.6.2 OpEmuRec

OpEmuRec is the official OPERA emulsion data analysis tool. Some algorithms are dedicated to reconstruction and data analysis and could work both on data and Monte Carlo files, others are dedicated to simulate the location procedure. The algorithm implemented in the OpEmuRec framework are:

- CSLNGS simulates the CS scanning and provide the CS candidate tracks to be connected in the brick.
- FEDRASCANBACK simulates the scanback procedure.
- FEDRALINK performes the linking beetwen the microtracks found in the two different emulsion layers in each films.
- FEDRAALIGN performes the alignment of the different films to analyzed.
- FEDRATRACK performes the tracking in the scanned volume.
- FEDRAVERTEX performes the vertex reconstruction.
- FEDRASHOWERING performes the shower reconstruction.
- MCSANNECY performes the momentum estimation of a track by means of the multiple coulomb scattering.
- SYSALALIGNFILTER is an alternative algorithm fro the linking and alignment

- SYSALTRACK is an alternative algorithm for tracking in the scanned volume.

- SYSALVERTEX is an alternative algorithm for the vertex recontruction.

The OpRelease file is a ROOT file structurated in trees. At the end of the analysis chain the following trees are contained in each OpRelease file:

- a tree with the list of the trees present in the file

- a tree with the Monte Carlo information and the electronic detector information.

- a tree for the brick finding algorithm

- 27 tree for Monte Carlo digits of the bricks around the neutrino interaction brick

- 27 tree for Monte Carlo digits of the CS around the neutrino interaction brick

- a tree with the segments found in the CS scanning

- a tree with the segments found in the scanback procedure

- a tree with the microtracks in the scanning volume

- a tree with the film to film alignment information

- a tree with a list of reconstructed tracks

- a tree with the reconstrcuted vertex

4.6.3 Results

In order to evaluated the location, reconstruction and identification efficiency of the standard procedure for ν_e and the possible gain of the dedicated procedure, a sample of:

- 1000 ν_e CC DIS with the energy distribution of the ν_e contamination of the beam,
- 1000 ν_e CC QE with the energy distribution of the ν_e contamination of the beam,
- 1000 ν_e CC DIS with the energy spectrum of the ν_μ of the beam,
- 3021 ν_μ NC.

has been analyzed. The events occur in the whole detector. The simulation consists of several step each simulating an action of the event analysis flow. First the events were processed by OpSim to propagate the particles through the detector and create their hits, and with OpDigit to simulate the detector responce. All the events left at least one digit in the detector apart from 21 ν_μ NC events, which have been discarded from the next steps of the anlysis.

The second step was to simulate the data acquisition trigger. It selectes only events on time with the beam and which had hits in the x and y projections of at least two TT planes or a TT plane with the sum of the photomultiplier signals exceeding 1500 ADC counts, and the presence of at least 10 hits. Subsequently the OpRec algorithm was applied and the OpCarac result was checked to know if the event was classified as “CONTAINED” or not. Only “CONTAINED” events were taken into account for the further steps of the analysis as done in data analysis. The result is shown in fig. 4.1.

Event type	ν_e CC (beam)	ν_e CC QE (beam)	ν_e CC (oscillated)	NC
Right Wall	0.92	0.88	0.87	0.82
Right Row	0.82	0.89	0.84	0.77
Right Column	0.86	0.90	0.85	0.79
Right Brick	0.68	0.71	0.63	0.56

Table 4.1: Efficiencies of the Brick Finding algorithm

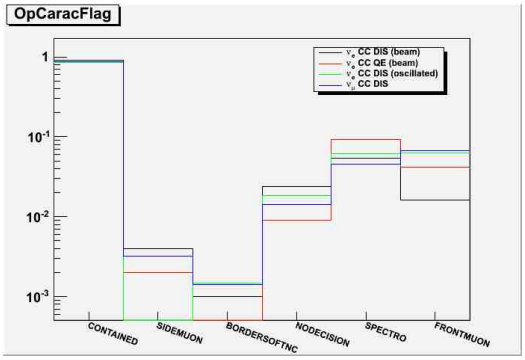

Figure 4.1: OpCarac Flag

In order to create the brick response the OpEmuIO algorithm was applied and for each event an array of $3 \times 3 \times 3$ bricks, around the brick where the interaction occured, was created. For each brick the microtracks in the brick emulsion and on the CS were simulated. Then the brick finding algorithm was applied and the result is shown in tab. 4.1.

Only the events in which the brick finding algorithm found the correct interaction brick were taken into account in the next steps of the simulation, while the others were discarded since the second and third brick analysis is not yet implemented in OpEmuRec. Then the CS results and CS-to-brick connection for the selected brick was checked as in the real case. Events without CS confirmation or without connections with the brick were discarded from the analysis. The distribution of the number of tracks found in the CSs

is shown in fig. 4.2

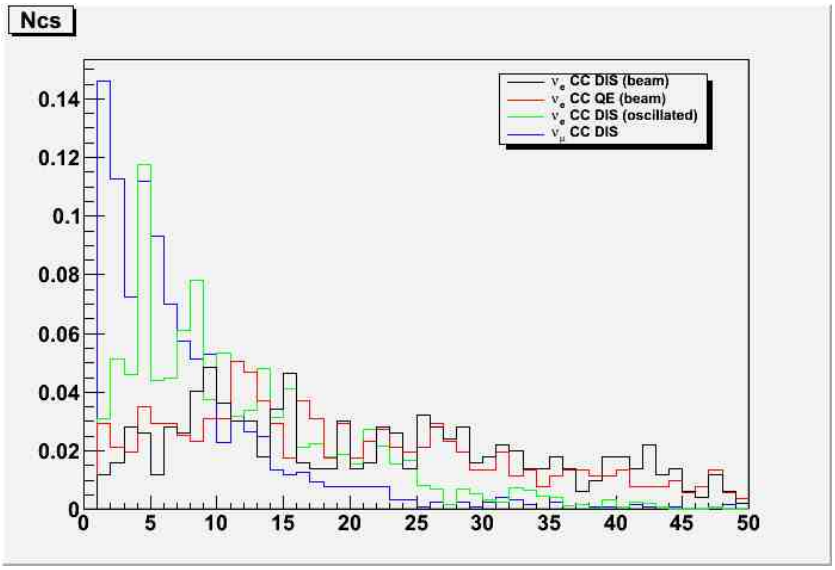

Figure 4.2: Number of found CS double basetracks

To localize the vertex, scanback procedure is performed. In fig. 4.3 and fig. 4.4 the X and Y residual between scanback stopping points and true Monte Carlo vertices are reported. In fig. 4.5 the Z residual, as a function of plate number is also reported.

Once the stopping point is reached, the scanning volume is defined as done in real data and the microtracks present in the volume are extracted and saved using OpEmuIO. To check if an event has been correctly located, the presence of the true neutrino interaction point is checked in a volume of 5 plates from the scanback stopping point. If the neutrino interaction point is outside the previous defined volume the event is considered as non located. To check if an event has been reconstructed, it is checked for the located events if the scanback track has been reconstructed. If the reconstructed scanback track is attached to an upstream vertex, the event is considered reconstructed as multiprong event otherwise as a single prong event. If the In fig. 4.6, fig. 4.7 and fig. 4.8 the residuals between the reconstructed vertex for multiprong events and true vertex position are shown.

Event type	ν_e CC (beam)	ν_e CC QE (beam)	ν_e CC (oscillated)	NC
Data acquisition trigger	1.0	0.997	1.0	0.940
Flagged as "CONTAINED" (OpCarac)	0.901	0.852	0.856	0.817
Right brick selected (Brick Finding)	0.616	0.608	0.541	0.461
CS Result	0.614	0.596	0.522	0.394
Successful CS to Brick connection	0.612	0.592	0.514	0.390
Successful Location	0.588	0.532	0.466	0.345
Successful Reconstruction	0.548	0.441	0.386	0.249

Table 4.2: Efficiencies for standard procedure

Fig. 4.9, fig. 4.10 and fig. 4.11 show the same histograms for events reconstructed as single prong.

With the event reconstruction the standard procedure was completely simulated. The results are shown in tab. 4.2, where the overall efficiencies for the standard procedure are reported together with the final location and reconstruction efficiencies for the different kind of event analysed.

In order to evaluated the possible gain in event location due to the dedicated procedure, the presence of the shower hint has been checked for not-located event. The presence of shower hints trigger the extension of the volume as previous explained. In the extented volume the shower reconstruction algorithm is performed in order to recosntructed the whole e.m. shower or at least part of it. When a shower is reconstructed it was checked if the primary of the shower is within 5 plates with respect of the true vertex. If it is the case the event is considered localized. The results are shown in tab 4.3.

As could be seen the ν_e dedicated procedure lead to an increase of the location efficiency of about 6% for the oscillated ν_e events and about 2% for

Event type	ν_e CC (beam)	ν_e CC QE (beam)	ν_e CC (oscillated)	NC
Not Localized	6.4%	15.1%	12.8%	14.1%
with shower hint	4.1%	10.4%	6.3%	6.6%
with a reconstructed shower	1.3%	3.7%	2.5%	0.7%
localized	1.1%	2.7%	1.8%	0.4%

Table 4.3: Efficiencies for extended procedure

Event type	ν_e CC (beam)	ν_e CC QE (beam)	ν_e CC (oscillated)	NC
Successful Reconstruction	54.8%	44.1%	38.6%	24.9%
with shower hint	53.3%	43.3%	33.4%	18.7%
with e.m. shower reconstructed	49.0%	41.6%	27.5%	10.3%
identified as ν_e	37.9%	40.2%	20.3%	4.4%
identified as ν_e (only multi prong vertex)	31.1%	2.5%	13.7%	4.2%

Table 4.4: Efficiencies for the ν_e identification

the prompt ν_e events.

For the localized event, the presence of the shower hint has been checked in order to trigger the e.m. shower reconstruction. If an event has a shower hint the shower reconstruction algorithm is performed. Then it is checked if the primary track of the shower is attached to the reconstructed vertex in order to discard shower originating from photons. If the primary track of the shower is attached the event is identified as a ν_e event. In tab. 4.4 is reported the identification efficiencies by means of the shower reconstruction tool, condidering all the reconstructed events or only multiprong events.

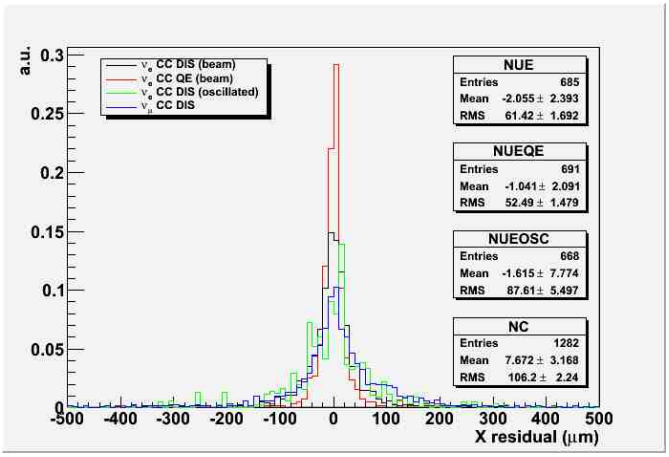

Figure 4.3: X residual

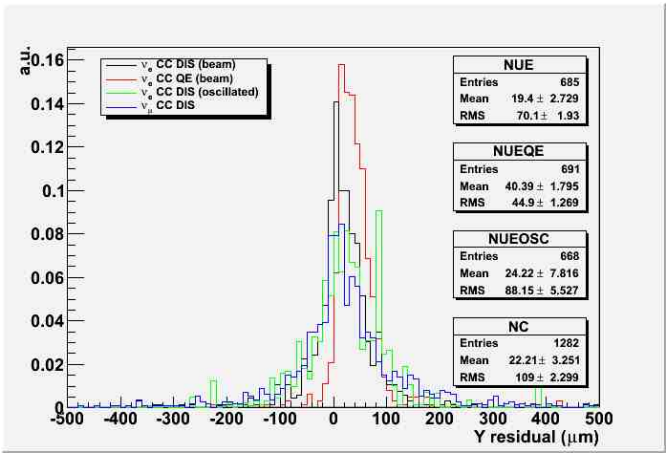

Figure 4.4: Y residual

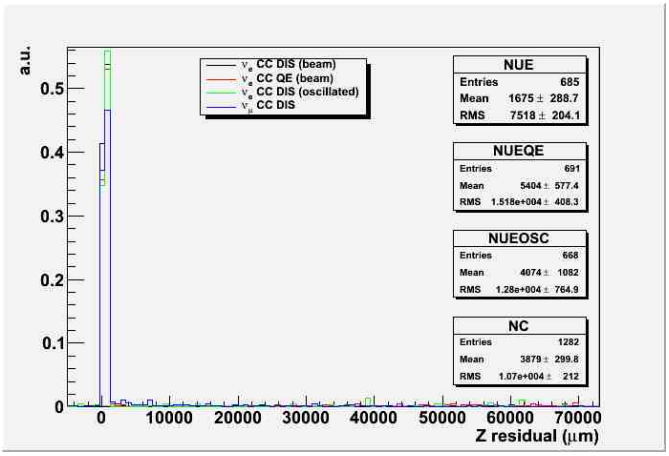

Figure 4.5: Z residual in term of plate

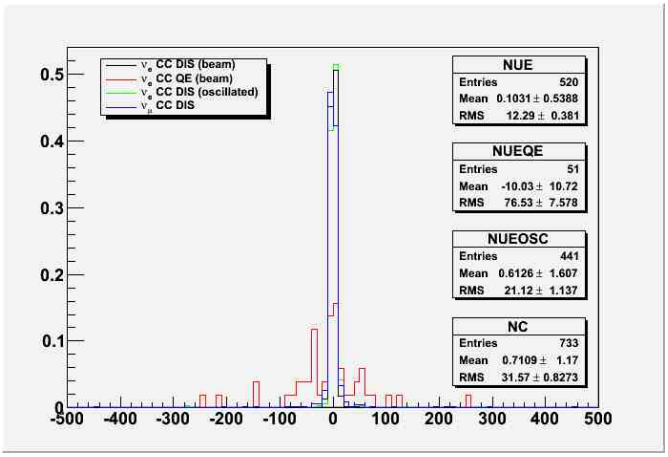

Figure 4.6: Residual beetween reconstructed vertex and true vertex in X position

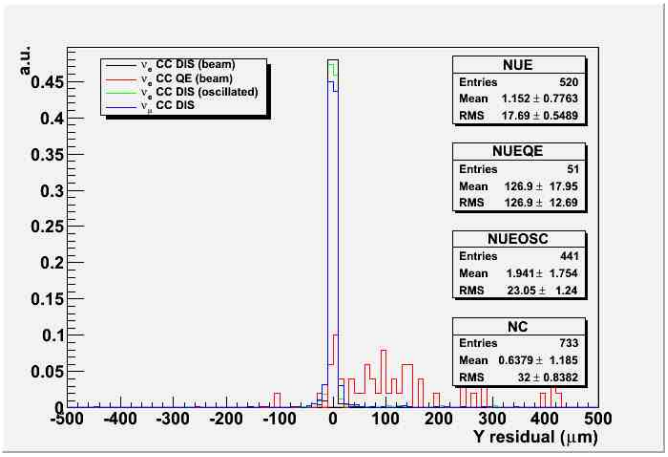

Figure 4.7: Residual beetween reconstructed vertex and true vertex in Y position

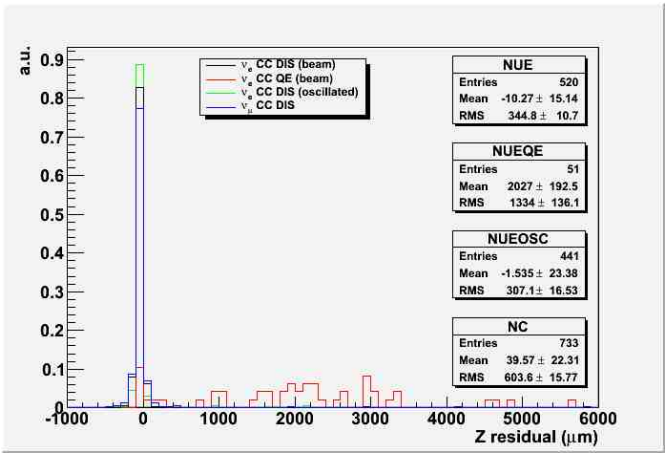

Figure 4.8: Residual beetween reconstructed vertex and true vertex in Z position

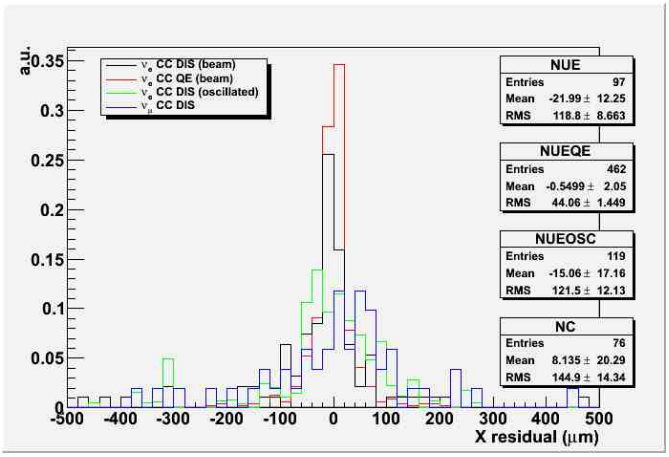

Figure 4.9: Residual beetween reconstructed vertex and true vertex in X position

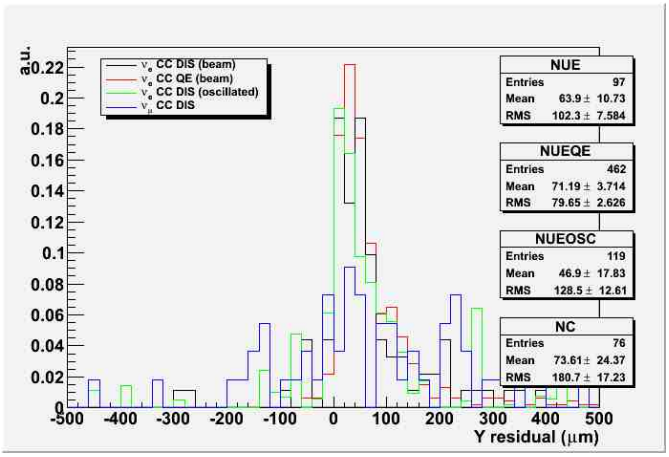

Figure 4.10: Residual beetween reconstructed vertex and true vertex in Y position

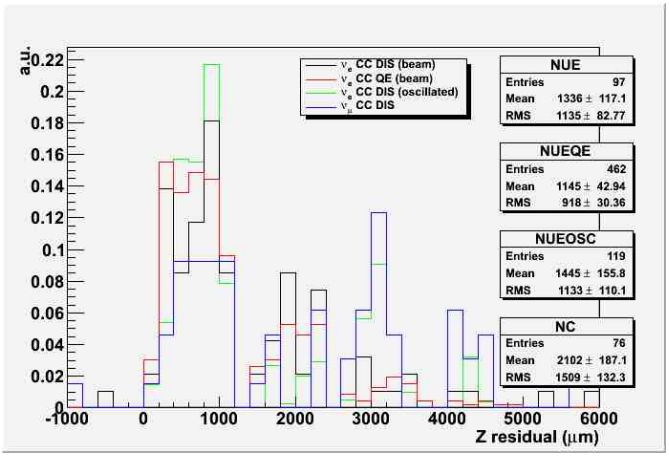

Figure 4.11: Residual beetween reconstructed vertex and true vertex in Z position

Chapter 5

Data Analysis

5.1 Data-MC Comparison for 0-μ events

In this section we validate Monte Carlo predictions using data of the 2008 and 2009 runs. The expected number of neutrino events registered in the target volume is 850 per 10^{19} p.o.t. per 1 *kton*. During the 2008 and 2009 runs the average target mass was 1.290 *kton*. The total number of p.o.t. was 1.78×10^{19} in 2008 and 3.52×10^{19} in 2009, respectively. With a trigger efficiency of 99% the total numbers of triggers in 2008 and 2009 on time with the beam amount to 10121 and 21455, respectively. About 85% of these are due to particles entering the target after being emitted in neutrino interactions occurring in the rock surrounding or in material inside the LNGS cavern. This component was identified during the 2008 run by performing a visual inspection of all on-time events. Events with topologies consistent with charged particles entering the detector or with low energy interaction of neutrons and γ-rays, mimicking a neutral current (NC) interaction, were discarded from the sample. For the 2008 data, stringent criteria were used guaranteeing a high level of purity at the cost of some inefficiency for very low activity events. A total of 1702 events was retained for the 2008 sample. In 2009, OpCarac algorithm was introduced in the data analysis. Its purpose is to automatically classify the events as explained in 4.6.1.

By applying the automatic selection algorithm on the 2009 sample 3629 events were expected from the simulation and 3693 were eventually selected from the experimental data. The sample was further reduced to 3557 events after visual inspection of the event displays. Data from the electronic detectors associated with the 5255 events reconstructed as occurring inside the target volume were processed by a software algorithm that selects the brick with the highest probability to contain the neutrino interaction vertex. This number can therefore be predicted by relying only on the size of the essentially uncontaminated 2008 sample. From the 1702 events constituting the 2008 sample, a fraction of about 5% of the events was rejected because occurring in bricks equipped with poor quality emulsion films, 1001 interaction vertices were located in bricks and 108 in the dead material, as shown in tab. 5.1, where CC and NC are separeted.

type	CC	NC
Selected events	1295	407
Good quality brick	1230	387
Located in the brick	835	166
Located in the dead material	88	20
Location efficiency	(75 ± 2)%	(48 ± 3)%

Table 5.1: Events of 2008 sample separated in CC and NC events and related location efficiencies.

Since in OpEmuRec only the most probable brick is taken into account we have to extrapolate the numbers quoted in Tab. 5.1 in which also the second and third probable bricks were used.

Taking into account that (75 ± 2)% of the total NC events has been located in the brick with highest probability evaluated by the Brick Finding, the location efficiency for the highest probability brick was estimated to be (36 ± 2)%, compatible with (37.4 ± 0.8)% obtained from the simulation ignoring the OpCarac classification. In Fig. 5.1 a comparison of the vertex

multiplicity and the vertex Z position inside the brick, between Monte Carlo ν_μ NC and 0-μ events from 2008 and 2009 data, are shown.

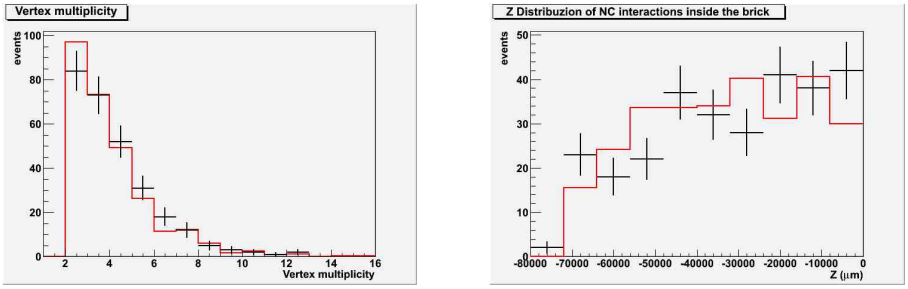

Figure 5.1: Left: Multiplicity distribution of reconstructed vertex for Monte Carlo ν_μ NC (black cross) and 0-μ events from 2008 and 2009 data (red line). The two distribution are qualitatively in agreement considering also that DecaySearch procedure, not implemented in Monte Carlo, increases the multiplicity of the events inducing a shift of the events on high multiplicity bins. Right: Distribution of the vertex Z position inside the brick for Monte Carlo ν_μ NC (black cross) and experimental 0-μ events from 2008 and 2009 data (red line). Monte Carlo well reproduce the trend of the data.

5.2 Evaluation of the expected ν_e event rate

Here we evaluate the expected rate of identified ν_e events. To identify a ν_e events, we apply the VertexToCS shower hint on the located 0-μ events. Then all the selected events are visually inspected on the emulsion film downstream the vertex in order to check if the selected track is showering or not. In this case an electron pair is searched to understand if the showers was originated from a gamma conversion.

First we evaluated the expected rate of identified ν_e due to the intrinsic contamination of the beam, according to the formula:

$$R_{\nu_e}^{beam} = N_A \times m \times \int \phi_{\nu_e}^{beam}(E) \times \sigma_{\nu_e} \times k \times \epsilon_{\nu_e}^{beam} \times \epsilon_{\nu_e}^{VertexToCS} \qquad (5.1)$$

where N_A is the Avogadro constant, m is OPERA detector mass that on average during the run 2008 and 2009 was 1290 tons, of which 8.6% of dead material other than lead plates and emulsion films. $\phi_{\nu_e(\overline{\nu}_e)}$ is the intrisic contamination of ν_e expected spectra, σ_{ν_e} is the CC ν_e cross section for an isoscalar target, k is a non-isoscalarity coefficient that for the OPERA target correspond 1.079, $\epsilon_{\nu_e}^{beam}$ is the location efficiency (4.2) scaled to consider also second and third brick, while $\epsilon_{\nu_e}^{VertexToCS}$ is VertexToCS hint efficiency find to be (77 ± 2) for ν_e events.

Then the expected rate of identified oscillated ν_e is evaluated according to the formula:

$$R_{\nu_e}^{oscillated} = N_A \times m \times \int \phi_{\nu_\mu}(E) \times P_{\nu_\mu \to \nu_e}(E) \times \sigma_{\nu_e} \times k \times m \times \epsilon_{\nu_e}^{oscillated} \times \epsilon_{\nu_e}^{VertexToCS} \tag{5.2}$$

where ϕ_{ν_μ} is the ν_μ spectra and $P_{\nu_\mu \to \nu_e}$ is the oscillation probability:

$$P_{\nu_\mu \to \nu_e}(E) = \sin^2 \theta_{13} \times \sin^2 \left(\frac{\Delta m^2 \cdot L}{4E} \right) \tag{5.3}$$

with $\sin^2 \theta_{13} = 0.1$ and $\Delta m^2 = 2.4 \times 10^{-3}$. The results are shown in Tab. 5.2.

type	Expected ν_e identification rate ν_e events/10^{19} p.o.t.
beam	4.2 ± 0.4
oscillated	0.36 ± 0.04
Total	4.6 ± 0.4

Table 5.2: Expected ν_e identification rate for ν_e events due to the intrinsic contamination of the beam and for oscillated ν_e events.

5.3 Background Evaluation

The expected background is mainly represented by ν_μ NC events with NC events with:

- $\pi^0 \rightarrow \gamma\gamma$ and at least one γ converted in the lead plate of the vertex
- Dalitz decays of the π^0
- charge exchange of π^-

and has been evaluated considering the fraction of ν_μ NC events with a single electron or two electron with position and slope within the emulsion resolution, leaving a basetrack, in the emulsion next to the neutrino interaction lead plate, pointing to the neutrino vertex with an impact parameter less than 10 μm. It has been found that (5.4 $\pm$ 0.2)% of the ν_μ NC events could be wrongly identified as ν_e events. So the expcted background rate as been evaluated according to the formula:

$$R_{BG} = \int \phi_{\nu_\mu}(E) \times \sigma_{\nu_\mu}^{NC} \times k \times m \times \epsilon_{\nu_\mu} \times \rho_{\nu_\mu}^{VertexToCS} \times \eta \qquad (5.4)$$

where ϕ_{ν_μ} is the ν_μ expected spectra, σ_{ν_μ} is the NC $\nu_\mu$cross section for an isoscalar target, ϵ_{ν_μ} is the location efficiency (4.2) scaled to consider also second and third brick, $\rho_{\nu_\mu}^{VertexToCS}$ is VertexToCS hint efficiency find to be (11 $\pm$ 2) for NC ν_μ events, while η is the fraction of NC events that represent the background as previously explained. So the expected background rate is evaluated to be (0.6 $\pm$ 0.1) events per 10^{19} p.o.t.

5.4 Data-MC Comparison for ν_e events

The number of 0-μ located events during the 2008 and 2009 runs is 522, corrisponding to 5.3 $\times$ 10^{19} p.o.t.; The event information about the topology of the event, needed for the application of the VertexToCS procedure, are available, in the central database, only for 505 events, corresponding to 96.7%

of the total sample. In this subsample, 90 events has been selected by the VertexToCS procedure. This events have to be visually inspected by means of the microscope, as previuosly explained, in order to discard hints due to γ mimics a primary electron. The check has been performed, at this moment, to 73 events corrisponding to 81.1% of all the selected events. Out of 73 selected events 18 has been confirmed to be a ν_e events. This sample corrisponds to 78.4% of the total 5.3×10^{19} p.o.t., i.e. 4.16×10^{19} p.o.t.. Therefore the expected number of identified ν_e events are:

$$N = (R_{BG} + R_{\nu_e}^{beam} + R_{\nu_e}^{oscillated}) \times 4.16 \cdot 10^{19} p.o.t. = 22 \pm 2 \qquad (5.5)$$

in agreement with the events found in the data.

5.5 Sensitivity Improvement

An higher signal-to-background ratio can be obtained once the kinematical analysis of each event is available [37]. A first improvement could be obtained measuring the visible energy of the event and discarding events with a visible energy smaller than 20 GeV. This cut will reduce the ν_e events due to the intrisic contamination of the beam as can be seen in Fig. 5.2.

On the other hand considering only events with the missing tranverse momentum at the primary vertex less than 1.5 GeV, it is possible to discard NC events and $\nu_\mu \rightarrow \nu_\tau$ events, having both a not detectable neutrino in the final state (see Fig. 5.3).

Exploiting this cuts a sensitivity in $sin^2\theta_{13}$ down to ~ 0.03 ($\Delta m^2_{23} = 2.5 \times 10^{-3}\ eV^2$ and $\theta_{23} = 45°$) can be achieved, as shown in Fig. 5.4.

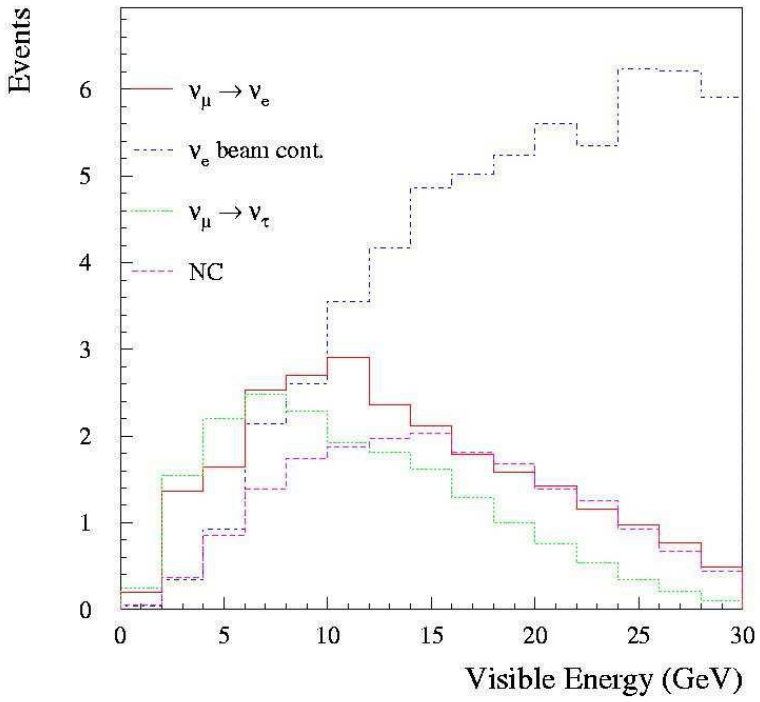

Figure 5.2: Visible energy distribution for oscillated ν_e events, ν_e from the beam, NC events and $\nu_\mu \rightarrow \nu_\tau$ events.

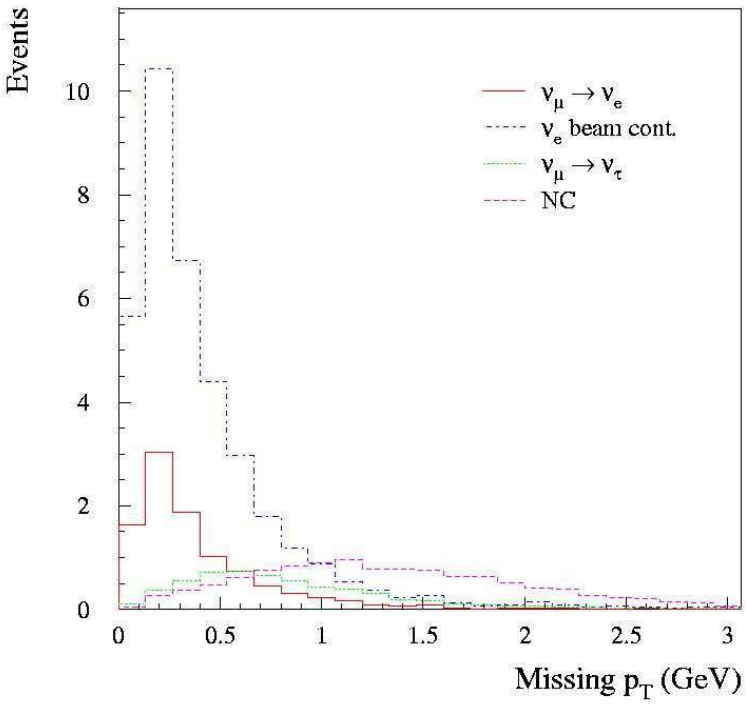

Figure 5.3: tranverse missing momentum at primary vertex for oscillated ν_e events and the other kind of events that mimick it.

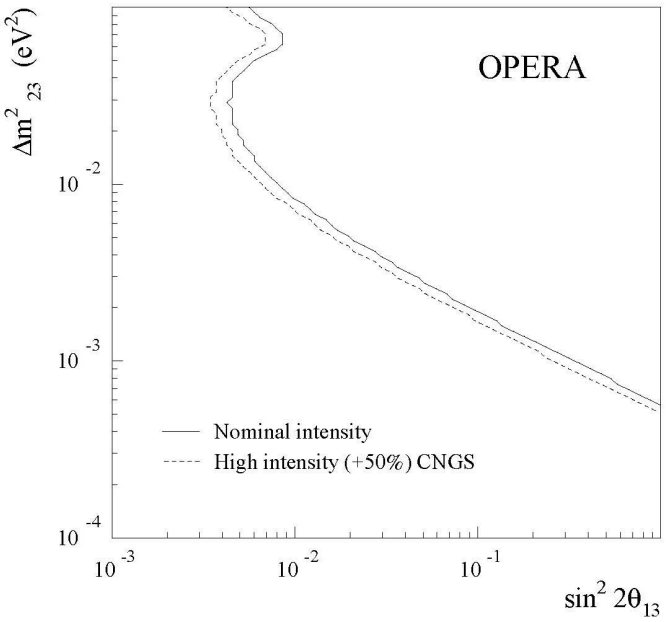

Figure 5.4: OPERA sensitivity to the parameter θ_{13} at 90% C.L. in a three family mixing scenario, in presence of $\nu_\mu \to \nu_\tau$ with $\theta_{23} = 45°$.

Conclusions

The OPERA experiment aims at the first direct observation of ν_τ appearance in an almost pure ν_μ beam, to univocally confirm the $\nu_\mu \rightarrow \nu_\tau$ oscillation hypothesis as explanation for the atmospheric neutrino deficit. The appearance signal is unfolded through the detection of daughter particles in the decay of the short-lived τ lepton produced in ν_τ CC interactions. A micrometric resolution is needed to study the topology of ν_τ induced events. The OPERA target is segmented in bricks, sandwich-like structures made of nuclear emulsion sheets interleaved with lead plates. 150000 bricks are arranged in vertical walls transverse to the beam direction. Plastic scintillator planes are suspended between brick walls, with the task to identify the brick where the neutrino interaction occurred, and magnetic spectrometers are used to eventually identify muons and measure their charge and momentum. Each brick is equipped with a Changeable Sheets (CS) doublet, a couple of emulsion films attached to the downstream side of the brick, allowinging to unambiguously confirm that the brick selected by the electronic detectors is the neutrino interaction one. The tracks found on CS doublet are then connected to that of the brick, projecting them in first films of the brick and searching for similar one with position and angular tollerances. The connected tracks are than followed back film by film with a procedure called scanback, in which segments of the tracks are searched starting from the previous measure and projecting it into the film under consideration. These procedure are optimazed for penetrating particle for which the straight line propagation is a good approximation. On the other hand it is less efficient

for less penetrating particles like electron. For this reason a new strategy has been defined in order to recover not located events with an electromagnetic shower in its final state. The new procedure is applied if the standard one is not successfull and if in the event is present an electromagnetic shower hint. A larger volume is scanned upstream the track showing the e.m. shower hint and the e.m. shower reconstruction algorithm is performed in order to recognize the shower or part of it. If the shower is not fully contained in volume, it is extended in the upstream direction till the whole shower is contained. The new procedure has been simulated in all the steps, using the OPERA ufficial software, with ν_e events from the beam and ν_e events from oscillation. The new procedure lead to an increase of the location efficiency of about 6% for the oscillated ν_e events and about 2% for the prompt ν_e events. Moreover the expected rate of ν_e events, due to ν_e from the intrinsic contaminatio, from $\nu_\mu \rightarrow \nu_e$ oscillation and from ν_μ NC background, has been evaluated taking into account the efficiency obtain by means of the simulation. With an equivalent p.o.t. of $4.16 \cdot 10^{19}$ the expected number of *nue* events for 2008 and 2009 is 22 ± 2, while 18 events has been identified in the data.

List of Figures

List of Tables

Bibliography

[1] J. Chadwick, *Intensitätsverteilung im magnetischen Spektren der β-Strahlen von Readium B + C*, Verh. d. D. Phys. Ges. **16** (1914), 383-391.

[2] C. D. Ellis, W. A. Wooster, *The Average Energy of Disintegration of Radium E*, Proc. R. Soc. Lond. **A117** (1927), 109-123.

[3] L. Meitner, W. Orthamann *Über eine absolute Bestimmung der Energie der primären β-Strahlen* von Radium E, Z. Phys. **60** (1930) 143-150.

[4] W. Pauli, *Letter to radioactive ladies and gentlemen at Tubingen conference*, 4th December 1930.

[5] J. Chadwick, *Letters to the editor: Possible existence of a nuetron*, Nature **129** (1932), 312.

[6] E. Fermi, *Tentativo di una teoria dei raggi β*, Nuovo Cimento **11** (1934), 1-19.

[7] C. L. Cowan, F. Reines, F. B. Harrison, H. W. Kruse and A. D. McGuire, *Detection of the Free Neutrino: a Confirmation*, Science **124** (1956), 103-104.

[8] M. Goldhaber, L. Grodzins and A.W. Sunyar, *Helicity Of Neutrinos*, Phys.Rev. **109** (1958) 1015-1017.

[9] G. Danby, J-M. Gaillard, K Goulianos, L. M. Lederman, N. Mistry, M. Schwartz and Z. Steinbergert, *Observation of high-energy neutrino*

interactions and the existence of two kinf of neutrinos, Phys. Rev. Lett. **9** (1962), 36-44.

[10] M. L. Perl *et al.*, *Evidence for Anomalous Lepton Production in* $e^+ - e^-$ *Annihilation*, Phys. Rev. Lett. **35** (1975), 1489-1492.

[11] N. Cabibbo, *Unitary Symmetry and Leptonic Decays*, Phys. Rev. Lett. **10** (1963), 531-533.

[12] M. Kobayashi and T. Maskawa, *CP-Violation in the Renormalizable Theory of Weak Interaction*, Prog. Theor. Phys. **49** (1973), 652-657.

[13] B. Pontecorvo, *Neutrino Experiments and the Problem of Conservation of Leptonic Charge*, Zh. Eksp. Teor. Fiz. **53** (1967), 1717-1725.

[14] Z. Maki, M. Nakagawa, and S. Sakata *Remarks on the Unified Model of Elementary Particles*, Prog. Theor. Phys. **28** (1962), 870-880.

[15] The ALEPH Collaboration, The DELPHI Collaboration, The L3 Collaboration, The OPAL Collaboration, The SLD Collaboration, The LEP Electroweak Working Group, The SLD Electroweak and Heavy Flavour Groups, *Precision electroweak measurements on the Z resonance*, Phys. Rept. **427** (2006), 257-454.

[16] K. Kodama *et al.*, (DONUT Collaboration), *Observation of tau neutrino interactions*, Phys. Lett. **B504** (2001), 218-224.

[17] L. Wolfenstein, *Neutrino oscillations in matter*, Phys. Rev. **D17** (1978), 2369-2374;
S. P . Mikheyev and A. Y. Smirnov, *Resonance Amplification of* ν *Oscillations in Matter and Solar Neutrino Spectroscopy*, Nuovo Cim. **C9** (1986), 17-26.

[18] M. Apollonio *et al.*, *Limits on neutrino oscillations from the CHOOZ experiment*, Phys. Lett. **B466** (1999) 415-430;

M. Apollonio *et al.*, *Search for neutrino oscillation n a long base-line at the CHOOZ nuclear power station*, Eur. Phys. J. **C27** (2003), 331-374.

[19] F. Boehm *et al.*, *Search for Neutrino Oscillations at the Palo Verde Nuclear Reactors*, Phys. Rev. Lett. **84** (2000), 3764-3767;
F. Boehm *et al.*, *Final results from Palo Verde neutrino oscillations experiment*, Phys. Rev. **D64** (2001), 112001.

[20] S. Yamamoto *et al.*, *Improved search for $\nu_\mu \to \nu_e$ oscillation in a long-baseline accelerator experiment*, Phys. Rev. Lett. **96** (2006), 181801.

[21] A. Aguilar *et al.*, *Evidence for neutrino oscillations from observation of $\overline{\nu}_e$ appearance in a $\overline{\nu}_\mu$ beam*, Phys. Rev. **D64** (2001) 112007.

[22] A. A. Aguilar-Arevalo *et al.*, *Event excess in the MiniBooNE search for $\nu_\mu \to \nu_e$ oscillations*, Phys. Rev. Lett. **105** (2010) 181801.

[23] J. Bahcall, A. M. Serenelli, S. Basu, *New solar opacities, abundancies, helioseismology, and neutrino fluxes*, Astrophys. J. **621** (2005) L85.

[24] R. Davis, Jr., D.S. Harmer, K.C. Hoffman, *Search for Neutrinos from the Sun*, Phys. Rev. Lett. **20** (1968) 1205-1209.

[25] GALLEX collaboration, W. Hampel *et al.*, *GALLEX solar neutrino observations: results for GALLEX IV*, Phys. Lett. **B447** (1999) 127;
SAGE Collaboration, J. N. Abdurashitov *et al.*, *Measurement of the solar neutrino capture rate with gallium metal*, Phys. Rev. **C60** (1999) 055801;
GNO Collaboration, M. Altmann *et al.*, *Complete results for five years of GNO solar neutrino observations*, Phys. Lett. **B616** (2005) 174.

[26] SUPER-KAMIOKANDE Collaboration, J. Hosaka *et al.*, *Solar neutrino measurements in Super-Kamiokande-I*, Phys. Rev. **D73** (2006) 112001.

[27] Q. R. Ahmad *et al.*, *Measurement of the rate of* $\nu_e + d \rightarrow p + p + e^-$ *interactions produced by* ^8B *Solar Neutrinos at the Sudbury Neutrino Observatory*, Phys. Rev. Lett. **87** (2001) 071301.

[28] J. N. Bahcall, *Solar Models: An Historical Overview*, Nucl. Phys. **B118** (Proc. Suppl.) (2003) 77.
J. N. Bahcall, *Solar Neutrinos. I. Theoretical*, Phys. Rev. Lett. **12** (1964) 300.

[29] KAMIOKANDE-II Collaboration, K.S. Hirata *et al.*, *Experimental Study of the Atmospheric Neutrino Flux*, Phys. Lett. **B205** (1988) 416.

[30] SUPER-KAMIOKANDE Collaboration, Y. Fukuda *et al.*, *Evidence for oscillation of atmospheric neutrinos*, Phys. Rev. Lett. **81** (1998) 1562.
SUPER-KAMIOKANDE Collaboration, J. Hosaka *et al.*, *Three flavor neutrino oscillation analysis of atmospheric neutrinos in Super-Kamiokande*, Phys. Rev. **D74** (2006) 032002.
SUPER-KAMIOKANDE Collaboration, K. Abe *et al.*, *A Measurement of Atmospheric Neutrino Flux Consistent with Tau Neutrino Appearance*, Phys. Rev. Lett. **97** (2006) 171801.

[31] SOUDAN-2 Collaboration, W.W.M. Allison *et al.*, *The atmospheric neutrino flavor ratio from a 3.9 fiducial kiloton-year exposure of Soudan 2*, Phys. Lett. **B449** (1999) 137.
SOUDAN-2 Collaboration, M.C. Sanchez *et al.*, *Observation of atmospheric neutrino oscillations in Soudan 2*, Phys. Rev. **D68** (2003) 113004.
SOUDAN-2 Collaboration, W.W.M. Allison *et al.*, *Neutrino oscillation effects in Soudan-2 upward-stopping muons*, Phys. Rev. **D72** (2005) 052005.

[32] MACRO Collaboration, S.P. Ahlen *et al.*, *Atmospheric neutrino flux measurement using upgoing muons*, Phys. Lett. **B357** (1995) 481.

MACRO Collaboration, M. Ambrosio *et al.*, *Measurement of the atmospheric neutrino-induced upgoing muon flux using MACRO*, Phys. Lett. **B434** (1998) 451. MACRO Collaboration, M. Ambrosio *et al.*, *Measurements of atmospheric muon neutrino oscillations, global analysis of the data collected with MACRO detector*, Eur. Phys. J. **C36** (2004) 323.

[33] KAMLAND Collaboration, T. Araki *et al.*, *Measurement of neutrino oscillation with KamLAND: evidence of spectral distortion*, Phys. Rev. Lett. **94** (2005) 081801.

[34] K2K Collaboration, M.H. Ahn *et al.*, *Measurement of Neutrino Oscillation by the K2K Experiment*, Phys. Rev. **D74** (2006) 072003.

[35] G. L. Fogli, E. Lisi, A. Marrone, A. Palazzo, A. M. Rotunno, *Evidence of $\theta_{13} > 0$ from global neutrino data analysis*, Phys. Rev. **D84** (2011) 053007.

[36] A Anokhina *et al.*, *Study of the effects induced by lead on the emulsion films of the OPERA experiment*, JINST **3** (2008) P07002.

[37] M Komatsu *et al.*, *Sensitivity to θ13 of the CERN to Gran Sasso neutrino beam*, J. Phys. G: Nucl. Part. Phys. **29** (2003) 443.